POLITECNICO DI MILANO
Scuola di Ingegneria Industriale e dell'Informazione
Laurea Magistrale in Ingegneria dell'Automazione

A randomized approach to the prediction of critical situations for air traffic due to uncontrolled space debris reentry

Relatore: Prof.ssa Ing. Maria Prandini

Tesi di Laurea di:
Alessandro Falsone, matricola 783988
Fabio Noce, matricola 786546

Anno Accademico 2012-2013

To everyone who supported us
during these past five years

Abstract

This thesis studies the problem of an uncontrolled reentry of a space debris and its possible impact on air traffic.
Whilst a controlled reentry occurs over the ocean or an uninhabited region where a no-fly zone can be timely issued, the precise time when an uncontrolled reentry occurs is hardly predictable in advance, and the debris may fall over a populated area with high air traffic density and cause fatalities on the ground as well as in the air. Interestingly, notwithstanding the fact that aircraft vulnerability is higher compared to that of people on the ground (even fragments weighting 300 grams only can cause a catastrophic event!), the aviation risk has started being considered only lately, being the risk for the population on the ground the main concern.
In order to limit service disruption and avoid fatalities in the air, it would be very useful to introduce automatic tools that, as soon as a debris enters the atmosphere, provide an estimate of the airspace area that will be occupied by the reentering debris (*debris footprint*) as well as of the actual risk to aviation. Air traffic controllers, who are in charge of monitoring air traffic and ensuring a safe flight, could then use these pieces of information to decide the best action in terms of aircraft re-routing and prioritization of the aircraft involved.
This work can be seen as a first step to achieve such an objective.
Inspired by some papers that have appeared recently in the literature, we adopt a probabilistic framework and describe the debris dynamics as well as air traffic through stochastic models. Given that the uncontrolled reentry of a spatial debris is affected by various sources of uncertainty (e.g., initial velocity, drag coefficient, wind), we formulate the problem of computing its 4-dimensional (space cross time) footprint as a chance-constrained optimization problem, where we minimize the size of the set that contains all the trajectories of the reentering debris, except for a fraction of predefined prob-

ability ε. This chance-constrained optimization problem is hard to solve, and here we head for a randomized solution based on constraint sampling, which is suboptimal but still guaranteed to be feasible with high probability. The proposed randomized method is shown to outperform a state-of-the-art approach resting on the linearization of the debris dynamics around a nominal trajectory.

We then investigate to what extent the availability of measurements of the debris position can decrease the size of the footprint, through the use of nonlinear filtering techniques and, in particular, of the Unscented Kalman Filter. A further improvement of the footprint is obtained by exploiting the radar measurements of the aircraft positions and applying Particle Filtering techniques to reduce the uncertainty on the wind affecting the debris trajectory.

Simulations are presented throughout the thesis to assess the performance of the proposed approaches. A concluding section suggests possible directions of future work.

Sommario

Questa tesi riguarda il problema del rientro non controllato di detriti spaziali ed il loro possibile impatto sul traffico aereo.
A differenza dei rientri controllati, che avvengono sopra l'oceano o sopra aree disabitate e che comportano una temporanea interdizione dello spazio aereo programmata con un certo anticipo, la finestra temporale in cui si verifica un rientro non controllato è difficilmente predicibile ed esso può interessare zone densamente abitate e caratterizzate da un'elevata densità del traffico aereo, ponendo a serio rischio sia le persone che sono a terra, sia quelle che sono in volo. Nonostante la vulnerabilità degli aerei sia maggiore rispetto a quella della popolazione al suolo (frammenti di appena 300 grammi possono causare delle catastrofi in quota), il problema del rischio per l'aviazione dovuto ad un rientro non controllato di un detrito spaziale è stato considerato solo in tempi recenti e comunque non studiato ancora a fondo come quello per la popolazione a terra.
Per evitare interruzioni protratte nel tempo del servizio aereo e soprattutto vittime, sarebbe molto utile avere a disposizione sistemi automatici che, a fronte del verificarsi del rientro di un detrito, stimano la regione dello spazio aereo coinvolta dal rientro (il cosiddetto footprint) ed il rischio a cui è sottoposto il traffico aereo. I controllori di volo, incaricati di monitorare il traffico e garantirne la sicurezza, potrebbero usare queste informazioni per decidere quale sia l'azione migliore da intraprendere per riorganizzare il traffico aereo nei settori coinvolti, suggerendo agli aerei variazioni opportune di rotta. Questo lavoro di tesi può essere considerato come un primo passo per raggiungere tale obiettivo.
Traendo ispirazione da alcuni articoli che sono apparsi di recente in letteratura, abbiamo adottato un approccio probabilistico per affrontare il problema, in cui le dinamiche di detrito e aerei sono descritte tramite opportuni modelli stocastici. Dato che un rientro non controllato è soggetto a varie fonti

di incertezza (ad esempio sulla velocità iniziale, la resistenza aerodinamica, ed il vento), abbiamo proposto di formulare il problema del calcolo del footprint come un problema di ottimizzazione soggetto a vincoli in probabilità (problema chance-constrained), dove si determina il footprint come l'insieme che contiene tutte le traiettorie del detrito ad eccezione di una frazione ε predefinita e piccola a piacere. I problemi di tipo chance-constrained sono particolarmente difficili da risolvere e qui abbiamo optato per un approccio randomizzato basato sul campionamento dei vincoli, il quale fornisce una soluzione sub-ottima (footprint non con volume minimo) che soddisfa il vincolo in probabilità del problema chance constrained originario. Il metodo proposto è stato confrontato con un approccio presentato in letteratura di recente e si è dimostrato ad esso superiore.
Successivamente abbiamo valutato come misure della posizione del detrito possano essere utilizzate per ridurre il volume del footprint, tramite tecniche di filtraggio non lineare (più precisamente l'Unscented Kalman Filter). Un'ulteriore riduzione di volume può essere ottenuta sfruttando le misure radar delle posizioni degli aerei e applicando il Particle Filter per ridurre l'incertezza riguardo l'effetto del vento sulla traiettoria del detrito. Viene inoltre proposto un metodo per stimare, seppure in modo conservativo, la probabilità che il detrito entri nella zona di sicurezza attorno ad un velivolo.

La tesi si sviluppa nel modo seguente.
Nel primo capitolo viene descritto il problema del rientro non controllato di detriti spaziali, sottolineando come esso sia stato affrontato solo di recente nell'ottica di valutare il rischio a cui è sottoposto il traffico aereo.
Nel secondo capitolo viene presentato in maniera accurata il problema della predizione della traiettoria di rientro dei detriti spaziali e le varie tecniche ad oggi utilizzate a tale scopo. In seguito viene introdotto e discusso il modello di caduta del detrito che verrà poi utilizzato in tutta la trattazione. Vengono inoltre evidenziate tutte le fonti di incertezza parametrica ed i diversi disturbi che possono influenzare la dinamica del rientro. Nella seconda sezione del capitolo si affronta il calcolo del footprint. Si mostra come sia possibile riformulare tale problema come un problema di ottimizzazione vincolata, con vincoli di natura probabilistica, che può essere risolto mediante l'impiego di tecniche randomizzate basate sulla simulazione. Il metodo proposto per il calcolo del footprint viene poi confrontato con un metodo recentemente

sviluppato in letteratura, rispetto al quale mostra prestazioni decisamente migliori. Nella parte conclusiva del capitolo si spiega come il footprint possa essere utilizzato per la stima del rischio per un aereo che si trova nello spazio coinvolto dal rientro non controllato.
La tesi prosegue con il capitolo 3, nel quale per prima cosa viene presentato il modello stocastico per la descrizione del traffico aereo. Vengono introdotte le equazioni che descrivono la dinamica del singolo velivolo, il flight management system ed il modello utilizzato per l'evoluzione della componente stocastica del vento. Vengono poi illustrate le possibilità offerte dall'avere a disposizione delle misure del detrito e degli aerei che si trovano nell'area interessata dal rientro. Vengono descritti gli algoritmi utilizzati per il filtraggio delle misure radar degli aerei (Sequential Conditioning Particle Filter – SCPF) e di quelle del detrito (Unscented Kalman Filtering – UKF). Successivamente viene introdotto un algoritmo che integra SCPF e UKF per il calcolo del footprint. Sulla base del footprint calcolato possono essere definite le regioni dello spazio aereo da interdire al traffico in opportune finestre temporali. Il capitolo 3 si conclude con esempi numerici che mostrano l'efficacia dell'approccio proposto. Nell'ultimo capitolo, infine, vengono tratte le conclusioni e suggerite alcune direzioni future di ricerca.

Acknowledgement

We would like to thank our families for supporting and encouraging us during these university years, our friends for enjoying time spent together, our classmates for wonderful five past years, our sweethearts for showing patience and always being close to us.
We also would like to thank Professor Maria Prandini for having involved us in this project and for working hard herself to make this accomplishment possible.

Ringraziamenti

Vorremmo ringraziare le nostre famiglie che ci hanno supportato e spronato in questi anni di studio, i nostri amici per le serate in compagnia, i momenti di svago e le chiacchiere, i nostri compagni per i meravigliosi cinque anni trascorsi insieme, le nostre dolci metà che hanno avuto molta pazienza e che ci sono sempre state vicine.
Vorremmo inoltre ringraziare la Professoressa Maria Prandini per averci coinvolto in questo progetto e per essersi spesa in prima persona per permetterci di portarlo a termine.

Contents

List of Figures

List of Tables

List of Algorithms

Chapter 1

Introduction

1.1 Context

Since the beginning of the space era the number of satellites grew significantly and so did the number of them which ceased their operations and now are orbiting around Earth without the possibility to be controlled from ground stations. Together with upper stage rocket bodies, and fragments generated by collisions with meteoroids or other artificial satellites, they constitute the so-called *space debris population*. When a debris orbit decays, mainly due to atmospheric friction, it can enter the atmosphere and pose risk to public safety, striking people and properties at ground. For this reason institutions like the Federal Aviation Administration (FAA) have defined standards for the calculation of the overall risk of a space mission and maximum admissible values for such a risk, see e.g. [42] and [3].
During a controlled reentry, the spatial debris is maneuvered so as to make it reenter the Earth's atmosphere avoiding high density fly zones and strike the ground in the ocean or over an uninhabited area. We instead have an uncontrolled reentry when the debris falls into the Earth's atmosphere and cannot be maneuvered so as to make it strike the ground in a desired point of the planetary surface. From the decay of the Sputnik 1 launch vehicle core stage on 1 December 1957 until 3 April 2013, 22142 catalogued orbiting objects have reentered the Earth's atmosphere. Currently, approximately 70% of the reentries of intact orbital objects are uncontrolled, corresponding to about 100 metric tons per year, and on average there is one spacecraft or rocket body uncontrolled reentry every week, with an average mass around 2000 kg [33].

Studies in the literature on uncontrolled reentries has ben focusing almost exclusively on the risk that the debris can cause to the population on the ground, [33, 7, 31, 16, 45], and only recently attention has been drawn on the impact on air traffic, [34, 5]. Fragments generated in the reentry process have a mass ranging from one gram to some thousand kilograms [3], and, while for the risk to the population on the ground only objects with high kinetic energy can cause damage, in the case of aircraft flying at speeds around 700 kilometers per hour, even an impact with a small debris, hypothetically at rest in the air, can cause severe damage to the aircraft and to passengers on board, [33].

In this work, we shall focus on the problem of uncontrolled reentry and its possible impact on air traffic. Since air traffic is experiencing an incredible growth and is forecasted to double in the next few decades, [4], this problem is becoming more and more significant.

In the current Air Traffic Management (ATM) system, coordination of air traffic is operated on two different time scales by the traffic flow management function and Air Traffic Controllers (ATCs). The traffic flow management function operates on a long term horizon by defining the flow patterns one-day ahead so as to ensure a smooth and efficient organization of the overall air traffic. ATCs operate on a short/mid term horizon of 10-20 minutes with the goal of maintaining the appropriate separation between aircraft and make them avoid forbidden regions, which may include special usage areas and bad weather zones, as well as the area occupied by a debris during its (uncontrolled) reentry. Indeed, expected reentry position and time can only be predicted quite approximatively. As a matter of fact todays prediction capability leave us with uncertainties in the order of ± 55 minutes from data available 6 hours before actual reentry event, moreover there is an inevitable delay (up to a few hours) between the obtained prediction and the public distribution of the results [31].

Hence coordination to avoid risk cannot be performed at the traffic flow management level, but only at the ATCs operation time scale.

It would then be useful to introduce some tool to support ATCs in performing their tasks when an uncontrolled space debris reentry occurs. Our thesis can be seen as a preliminary step in this direction.

1.2 Objectives

This work pursues the goal of constructing hazard airspace areas of a reentering debris at different altitudes and their time duration, so as to support air traffic controllers in their task of guiding safely aircraft from their origin to their destination. In particular, given the various sources of uncertainty affecting the debris reentry, we aim at characterizing the reentry process probabilistically, determining the 4-D (space cross time) confidence region that will be occupied by the debris during its reentry. The risk of an aircraft getting too close to a reentering debris can be estimated based on this *probabilistic footprint*, and aircraft can be ranked based on the estimated risk. Air traffic controllers could then exploit these pieces of information for taking appropriate actions so as to make the aircraft avoid the 4-D confidence regions occupied by the falling debris, while assigning to the aircraft priorities according to their rank. Choice of the level of confidence will allow to modulate the size of the confidence regions.

1.3 Contribution and structure

A novel contribution of this thesis is the reformulation of the problem of determining the debris footprint as a chance-constrained optimization program, where one looks for the minimum size region that contains all debris trajectory except for a fraction of predefined probability ε, and the introduction of a simulation-based approach for its solution. This approach rests on the so-called *scenario approach*, [14], for (approximately) solving chance-constrained optimization programs through randomization of the probabilistic constraint.

The resulting randomized algorithm for footprint calculation is shown to outperform a state-of-the-art approach named covariance propagation, and to be of more general applicability.

When radar measurements of the aircraft and debris are available, nonlinear filtering techniques can be adopted to reduce the uncertainty affecting the debris reentry and, hence, the size of the probabilistic footprint. More precisely, we investigate the combination of the Unscented Kalman Filter (UKF, [24]) and the Sequential Conditioning Particle Filter (SCPF, [26]), respectively using the debris measurements to reduce the parametric uncertainty and the aircraft measurements to reduce the uncertainty on the

stochastic wind disturbance.
In Chapter 2 we present a brief overview of current challenges and solutions to the problem of debris trajectory modeling during reentry, and describe the model adopted in our work, listing the sources of uncertainties that affect it. Then, we introduce a novel simulation-based method for the debris footprint characterization, and show that it outperforms a method recently proposed in the literature. At the end of the chapter we discuss how the footprint can be used to obtain an upper bound for the aircraft risk.
In Chapter 3, we recall a recently proposed model for the air traffic, which includes a description of the uncertainty affecting the aircraft dynamics caused by the random nature of the wind speed. We then present the SCPF and the UKF algorithms separately, and show how they can be used jointly, so as to reduce the debris dispersion and determine an improved debris footprint. At the end of the chapter, we illustrate some simulation results obtained by the proposed approach, which integrates nonlinear filtering within the chance constrained program for the footprint calculation.
Finally, in Chapter 4, we draw some conclusions and suggest some directions for future research studies.

Chapter 2

Space debris and footprint characterization

2.1 Introduction

In this chapter we describe the uncontrolled space debris reentry phenomenon, and briefly illustrate modeling challenges and approaches proposed in the literature. We then focus on a model for trajectory prediction after the break-up instant, and illustrate the various sources of uncertainty affecting the debris trajectory. Based on this model, we characterize the debris dispersion probabilistically, by constructing the 4-D (space cross time) confidence region that will be occupied by the debris during its reentry. Knowledge of debris hazard regions and their time duration would simplify the air traffic controllers task of guiding the aircraft away from the hazard area before the debris would reach the altitude at which aircraft are flying. Additionally, the probabilistic footprint could be used to provide an estimate of the risk posed to air traffic by the debris reentry, and to assign a ranking to the aircraft based on the estimated individual risk.
The main novel contribution of this chapter consists in the introduction of a simulation-based approach to the construction of the debris probabilistic footprint. The approach rests on recent results on the randomized solution to chance constrained optimization problems, and shows better performance when compared with a state-of-the-art method.

2.2 Reentry of a space debris: modeling

2.2.1 Modeling challenges and state of the art

Up today, accurate and reliable models to describe space debris reentry are not available yet, and many researchers are actively working on this problem. The motivation is that reentry dynamics is a very complex phenomenon.
A manmade satellite that has been sent into orbit, once its mission is completed, can perform two different kinds of reentry: a targeted or *controlled* reentry, or a random or *uncontrolled* reentry. While in the first case the object has been explicitly designed to survive the reentry phase, and its trajectory has been planned so as to make it fall into the ocean or in an unpopulated land, in case of an uncontrolled reentry, an object orbiting around the Earth with an inclination i with respect to the equatorial plane, can fall anywhere in a latitude range $\pm i$, [31, 34], posing at risk both people on the ground and aircraft in flight.
Though it is difficult to predict when and where a reentering satellite will strike the ground, we do have instruments to observe and track orbiting object [31]. Data about space debris population are issued through the TLEs (Two-Line Elements) database, which contains mainly orbital parameters: orbital inclination with respect to the equatorial plane, the right ascension of the ascending node and the argument of perigee uniquely defining the orbit, the mean anomaly specifying the position along the orbit, and the mean motion specifying the mean angular speed. Monitoring these information is important, because they can be used to properly initialize an *orbit propagator* model and predict the trajectory of the reentering body. Unfortunately, these models depend on the Earth gravitational field and on the exosphere density, which are affected by approximation errors, and TLEs data are often sparse and poorly accurate. Recent works, like [21], propose new techniques to constantly monitor space debris population, at least for LEO (Low-Earth Orbit) objects, and we believe that new technologies will make us able to raise the accuracy of the available measurements. Other works, also with different aims, like [40], show how orbital propagators can be improved considering more accurate models.
When a satellite ceases its operations typically continue to orbit around the Earth until atmospheric drag reduce its speed making it lower its semi-major axis. At this time the object is already in a decaying orbit, but the reentry

phase begins when the body intersect the entry interface, that is the top of sensible atmosphere (i.e. at an altitude of 120 km). This instant if often referred as reentry epoch and is often taken as the reference time for debris trajectories [5]. Typical speed of an orbiting satellite is about 7 km/s and, as it passes the reentry interface, it encounters a steadily increasing atmospheric density and it begins to heat due to aerodynamic drag. Since each material has its own melting point, as temperature increase, we have a sequence of failure at different points, each time the object release one or more parts and each of these fragments falls independently on its own trajectory. Moreover we can have other mechanical failures due to increasing aerodynamic loads that can reach seven or more times the acceleration of gravity [5]. Since each fragment has its own mechanical and thermal properties, it can generate other fragments or it can ablate, partially or completely. Of course completely ablated fragments do not contribute to risk evaluation, but all other fragments will affect the projected range of hazardous areas. All fragments evolve with a ballistic trajectory, only subject to gravity and aerodynamic forces [45, 16]. Though this fragmentation is far from instantaneous we refer to it as *breakup instant*, meaning the instant when the reentering body experiences a major breakup (i.e. the first massive breakup) after it has passed the reentry interface. Currently, there are two strategies to predict this breakup instant of a reentering satellite: a deterministic approach and a probabilistic one.

In [46] the authors summarize all current tools[1] and methods to predict breakup instant, while proposing their own tool. These softwares can be classified as object-oriented or spacecraft-oriented. In the first case the software can simulate a three degrees of freedom ballistic model, attitude equations are typically predefined based on the chosen shape for the object and so are not directly integrated, aerodynamic load and heating are integrated in all the three regimes (free molecular flow, continuum flow and transitional regime) and ablation analysis can be carried out both using a lumped-mass or a distributed approach. Since the structural analysis is omitted, because the software deals with single objects only, breakup event cannot be predicted and it is assumed to occur at a given altitude, typically 78 km. A spacecraft-oriented code is instead much more complex, the entire structure of the satellite is reproduced as realistically as possible. Starting from a few

[1] Most of them are proprietary and so they cannot be used in this study.

elementary components (the primitives) composing the spacecraft and organizing all subsystems hierarchically, a full six degrees of freedom model is used to perform numerical integration for both position and attitude, a two-dimensional heat conduction approach is used for ablation analysis and, finally, aerodynamic forces and torques are integrated over all surfaces. Most fragile parts are monitored for both melting and mechanical overload, in order to be able to determine what kind of fragment is generated and when.
A totally different approach is the one carried out in [45, 16] where, instead of a very complex and purely deterministic model, a very simple model is used and probabilistic distribution are defined to account for the lack of knowledge about model coefficients and for the stochastic nature of the disturbances affecting the reentry process. Basically, a two-degrees of freedom kinematic model describing the debris motion along with a lumped-mass model describing the heating process are used to simulate different scenarios corresponding to sampled values of the uncertain parameters, and the probability of breakup of each fragment is then obtained. Breakup criteria cover only thermal melting and not mechanical stress.

2.2.2 Adopted model

Following [5], which suggests that the spread of debris footprint caused by breakup altitude uncertainty can be reduced if the object is observed during the major breakup, we focus only on fragment dispersion *after* the breakup phase, and adopt the three-degrees of freedom model of a falling object over a rotating planet recently proposed in [39] to this purpose. Thermal analysis for breakup prediction is not considered here, though the lumped-mass model describing the heating process in [45, 16] could be easily integrated in the adopted kinematic model.
Now we describe the model, drawing equations and presenting underlying hypothesis and limitations. Later on in this section we show what kinds of uncertainties affect the considered model.
Let $\boldsymbol{x} = [x, y, z]^T$ represent the position of the falling fragment with respect to a topocentric horizon coordinate system at the breakup instant. The frame, from now on called ENZ (East-North-Zenith), is centered at (ϑ_0, φ_0) on the Earth's surface (initial longitude: ϑ_0; initial latitude: φ_0), the xy plane is the local horizon (i.e. the plane tangent to Earth at the origin), the x-axis points eastward, the y-axis points northward and the z-axis is

directed towards the zenith. In this way, fragment reentry after breakup has $\boldsymbol{x}_0 = [0, 0, z_0]^T$ as initial position, with z_0 representing the altitude of breakup.
With reference to the ENZ frame just outlined, the equations of motion describing the debris trajectory are given by, [39]:

$$\dot{\boldsymbol{x}} = \boldsymbol{v} \tag{2.2.1a}$$

$$\dot{\boldsymbol{v}} = -\boldsymbol{a}_d - g\boldsymbol{e}_3 - 2\boldsymbol{\omega} \times \boldsymbol{v} - \boldsymbol{\omega} \times [\boldsymbol{\omega} \times (\boldsymbol{x} + R_e \boldsymbol{e}_3)] + \boldsymbol{\xi} \tag{2.2.1b}$$

where $\boldsymbol{v} = [v_x, v_y, v_z]^T$ is the velocity, $\boldsymbol{a}_d$ is the atmospheric drag deceleration, $\boldsymbol{\omega} = [0, \omega_e \cos(\varphi_0), \omega_e \sin(\varphi_0)]^T$ is the angular velocity vector of the ENZ frame (Earth's rotation rate: $\omega_e = 7.2921 \times 10^{-5}$ rad/s) and $\boldsymbol{e}_3 = [0, 0, 1]^T$. Constant R_e is the Earth's mean radius ($R_e = 6.3728 \times 10^6$ m), whereas if we assume an inverse square gravity model, the gravitational acceleration is given by

$$g = g_g \left(\frac{R_e}{R_e + z} \right)^2,$$

where $g_g = 9.81$ m/s^2 is the gravitational acceleration on the ground. Note that in this model gravity acceleration vector is assumed to be directed along the z-axis, and this could be a strong assumption if the reentering object has a long ground track. Let the ballistic coefficient β be given by

$$\beta = \frac{m}{C_d A}, \tag{2.2.2}$$

where m is the mass of the debris, A its cross-sectional area, and C_d the aerodynamics coefficient. Then, the atmospheric drag deceleration $\boldsymbol{a}_d$ acting on the fragment can be expressed as

$$\boldsymbol{a}_d = \frac{1}{2} \frac{\rho(z)}{\beta} v_r \boldsymbol{v}_r, \tag{2.2.3}$$

where $\rho(z)$ is the atmosphere density as a function of the altitude, $\boldsymbol{v}_r = \boldsymbol{v} - \boldsymbol{w}$ is the debris speed relative to the wind velocity $\boldsymbol{w}$, and $v_r = \|\boldsymbol{v}_r\|$ is the magnitude of $\boldsymbol{v}_r$.
Finally, $\boldsymbol{\xi}$ is a random acceleration vector that accounts for modeling uncertainties and disturbances. In [39], $\boldsymbol{\xi}$ is first assumed to have a Gaussian distribution, and then neglected in the study carried out by the authors.

2.2.3 Uncertainties affecting the reentry trajectory

Observations have shown that the major breakup event happens at an altitude of about 78 km [5] with an uncertainty range from ± 10 to ± 20 km [45, 16, 31]. So, fragments generated from this first breakup are distributed over a range of altitudes, thus increasing the spread of debris footprint along the direction of motion. This kind of uncertainty, as we said earlier, can be reduced if the object is observed during the major breakup [5].
Besides the complex nature of the breakup process, even post-breakup trajectories of various fragments are subject to strong uncertainties. In equation (2.2.3) we can see that the expression of the aerodynamic drag depends on a few parameters that are mostly unknown. The first thing to notice is the dependence of this expression from the atmospheric density, which is a function of altitude. Although several models have been employed [40], studies show that results are quite sensitive to the model chosen to describe the atmosphere, thus making atmosphere mismodeling an important source of uncertainty [33].
Moreover, since we are dealing with post-breakup fragments, we do not know exactly the mass, the cross-section nor the aerodynamic coefficient, which all enter the ballistic coefficient through equation (2.2.2). Just to give an example of the extent of the uncertainty that affects β, consider the three campaigns of reentry prediction that were carried out recently, one for each of the three massive spacecraft, UARS, ROSAT and Fobos-Grunt. These campaigns offered the opportunity to determine the evolution of the ballistic coefficient of spacecraft characterized by quite different configurations and shapes. Results of these campaigns are mentioned in [7, 32], where it is shown that the variability of β even prior to th breakup event can be up to 20%. This variability of β is likely to affect the time available to issue a warning to the aircraft for their safety, [5]. All this motivates the choice in e.g. [45, 16] to adopt a probabilistic approach and assume some sensible probability distribution for β.
Also the local wind, that depends on where and when the reentry takes place, is pointed out as a source of uncertainty, [3, 5], due to its effect on debris trajectories after the breakup process, when the debris enters the low atmosphere. The horizontal component of the velocity vector is in fact typically dominated by the wind that can cause a cross-track dispersion of the debris, [5]. The effects of this stochastic disturbance are more visible on

those fragments that has a lower ballistic coefficient, [3].
It is worth noticing that uncertainties affecting the ballistic coefficient as well as the position and velocity at the breakup instant and the wind disturbance can be easily incorporated in the adopted model (2.2.1).
Other sources of uncertainty that affects the atmospheric model (and, hence, the debris dynamics), such as geomagnetic activity, luny-solar perturbations, and solar radiation are not considered in this work, but are discussed in [7, 32, 31].

2.3 Probabilistic footprint

We next present a probabilistic approach to determine the footprint of a debris fragment, which allows to account for the various sources of uncertainty affecting the reentry trajectory.
Our goal is to determine the minimum size 4D region of the airspace where all trajectories except a set of predefined probability ε are confined. This can be formulated as a chance-constrained optimization problem and we propose here to solve it through a randomized method. The resulting approach to determine the 4D footprint rests on running multiple realizations of the reentry trajectory and imposing that they belong to the footprint. For this reason, we call it *simulation-based method*.
We compare the proposed simulation-based method with the analytic *covariance propagation method* recently proposed in [39]. The two approaches are described in Sections 2.3.1 and 2.3.2, and then compared in Section 2.3.3. Finally, in Section 2.3.4, we illustrate the possibility of using the probabilistic footprint for estimating the risk caused to air traffic by an uncontrolled debris reentry.

2.3.1 A novel simulation-based method

In this section, we describe the proposed simulation-based approach to determine the debris footprint. We shall first start from the problem of characterizing the debris dispersion at a certain time instant (3D footprint), and then generalize the approach to 4D (space cross time).

3D debris footprint

We adopt an ellipsoid to describe the debris dispersion at a certain time instant t and look for the ellipsoid

$$\mathcal{E}_\varepsilon = \{\boldsymbol{x} \in \Re^3 : \ (\boldsymbol{x} - \boldsymbol{c})^T A (\boldsymbol{x} - \boldsymbol{c}) \leq 1\}$$

with the minimum volume that contains all possible debris trajectories except for a set of probability at most ε.
This can be formalized in terms of the following chance-constrained optimization problem:

$$\begin{aligned} \min_{A,\boldsymbol{c}} \quad & \sqrt{\det A^{-1}} \\ \text{subject to:} \quad & A = A^T \succ 0 \\ & \mathcal{P}\left\{\delta \in \Delta : \ (\boldsymbol{x}_\delta(t) - \boldsymbol{c})^T A (\boldsymbol{x}_\delta(t) - \boldsymbol{c}) \leq 1\right\} \geq 1 - \varepsilon, \end{aligned} \tag{2.3.1}$$

where $\boldsymbol{x}(t)$ denotes the position of the debris at time t, whereas the optimization variables $\boldsymbol{c}$ and A respectively represent the center of the ellipsoid and the positive definite symmetric matrix defining its shape.
Position $\boldsymbol{x}(t)$ is affected by various sources of uncertainty and here we make it explicit by using the notation $\boldsymbol{x}_\delta(t)$, where δ is the uncertainty vector taking values in the uncertainty set Δ according to the probability distribution $\mathcal{P}$. Vector δ allows to account for parametric uncertainties and disturbances affecting the reentry trajectory, that is, initial velocity, ballistic coefficient, breakup altitude, and the wind disturbance, as described in Section 2.2, as long as they are characterized through some probability distribution function.
If we let $(A^\star, c^\star)$ be the solution to (2.3.1), then

$$\mathcal{E}_\varepsilon^\star = \{\boldsymbol{x} \in \Re^3 : \ (\boldsymbol{x} - \boldsymbol{c}^\star)^T A^\star (\boldsymbol{x} - \boldsymbol{c}^\star) \leq 1\}$$

is the minimum volume ellipsoid that represents the 3D footprint associated with the violation parameter ε.
Chance-constrained optimization problems are known to be difficult to solve [36, 37], except for specific cases like when the involved probability distribution is Gaussian. We next show how to approximately solve problem (2.3.1) via a randomized method, called the *scenario approach*, [9, 10, 13, 11, 14],

which reduces the chance-constrained optimization problem to an optimization problem with standard (i.e., non probabilistic) constraints, while providing guarantees on the chance-constrained feasibility of the obtained solution. To this purpose we need first to reformulate problem (2.3.1) so that the cost function to be minimized is convex with respect to the optimization variables. Convexity of both the cost and of the set appearing under the probability $\mathcal{P}$ in the chance-constraint is in fact needed for providing theoretical guarantees on the quality of the scenario solution.
Problem (2.3.1) can be rewritten as follow:

$$\begin{aligned} \min_{A,\boldsymbol{c}} \quad & \log\det A^{-1} \\ \text{subject to:} \quad & A = A^T \succ 0 \\ & \mathcal{P}\left\{\delta \in \Delta :\ (\boldsymbol{x}_\delta(t) - \boldsymbol{c})^T A\,(\boldsymbol{x}_\delta(t) - \boldsymbol{c}) \leq 1\right\} \geq 1 - \varepsilon, \end{aligned} \tag{2.3.2}$$

where, indeed, the cost $\log\det A^{-1}$ is convex as a function of A, [8].
The main concept of the scenario approach is that solvability of the optimization problem (2.3.2) can be achieved by extracting a finite number N of realizations of the uncertainty parameter δ and replacing the constraint in probability with the N constraints associated with the extracted δ's uncertainty instances.
This leads to the following convex optimization problem with a finite number of constraints:

$$\begin{aligned} \min_{A,\boldsymbol{c}} \quad & \log\det A^{-1} \\ \text{subject to:} \quad & A = A^T \succ 0 \\ & (\boldsymbol{x}_{\delta^{(i)}}(t) - \boldsymbol{c})^T A\,(\boldsymbol{x}_{\delta^{(i)}}(t) - \boldsymbol{c}) \leq 1,\ i = 1, 2, \ldots, N, \end{aligned} \tag{2.3.3}$$

where $\delta^{(i)}$, $i = 1, \ldots, N$ are extracted independently from Δ according to the distribution $\mathcal{P}$.
As opposed to (2.3.2), (2.3.3) is a *convex* optimization problem with a *finite* number of constraints and can be addressed via available solvers provided that N is not too big.
The resolution of (2.3.3) is not straightforward [43] due to the log function appearing in the cost. Here, we adopt a solution where first the convex hull of all data points $\boldsymbol{x}_t\left(\delta^{(i)}\right)$ is computed, and then Khachiyan's algorithm is applied, [44, 43].

The fact that the scenario solution is feasible also for the original problem is guaranteed by the following theorem, whose proof is given in [13].

Theorem 1. *Select a "violation parameter" $\varepsilon \in (0,1)$ and a "confidence parameter" $\eta \in (0,1)$. If N is such that*

$$\sum_{i=0}^{d} \binom{N}{i} \varepsilon^i (1-\varepsilon)^{N-i} \leq \eta \tag{2.3.4}$$

where d denotes the number of optimization variables in (2.3.3), then, with probability no smaller than $1-\eta$, the solution $(A_N^\star, \boldsymbol{c}_N^\star)$ to the scenario optimization problem (2.3.3) satisfies

$$\mathcal{P}\left\{\delta \in \Delta : \ (\boldsymbol{x}_\delta(t) - \boldsymbol{c}_N^\star)^T A_N^\star (\boldsymbol{x}_\delta(t) - \boldsymbol{c}_N^\star) \leq 1\right\} \geq 1-\varepsilon.$$

Remark 1. Note that, with respect to the original bound in [13], (2.3.4) presents $d+1$ in place of d. This is because the bound in [13] refers to a chance-constrained optimization problem with a cost function that is linear in the optimization variables. To reduce our setting to that in [13], we should then add an additional optimization variable h and adopt the following reformulation of (2.3.3):

$$\begin{aligned} \min_{A,\boldsymbol{c},h} \quad & h \\ \text{subject to:} \quad & A = A^T \succ 0 \\ & (\boldsymbol{x}_{\delta^{(i)}}(t) - \boldsymbol{c})^T A (\boldsymbol{x}_{\delta^{(i)}}(t) - \boldsymbol{c}) \leq 1, \, \forall i = 1,2,\ldots,N, \\ & \log\det A^{-1} \leq h. \end{aligned} \tag{2.3.5}$$

A similar consideration holds for the bound in Theorem 2. □

Note that the results on the feasibility of the scenario solution holds with a certain confidence $1-\eta$. This is because the scenario solution depends on the extracted uncertainty instances and it may then happen that a bad multi-sample (e.g., all $\delta^{(i)}$'s equal) is extracted and the feasibility property does not hold. However, this becomes more and more unlikely ass N increases and the probability η of this unfortunate event can be set as small as 10^{-10} (i.e., zero in practice) without growing too much the sample size N. Indeed,

the explicit bound for N satisfying (2.3.4)

$$N \geq \frac{d+1+\ln(1/\eta)+\sqrt{2(d+1)\ln(1/\eta)}}{\varepsilon}$$

derived in [6] shows that the dependence on η is logarithmic.
Note that though extremely powerful, this randomized approach may lead to conservative results, i.e., to a solution with an actual violation that is much smaller than ε. This is quite intuitive: it is possible that a few "outliers" causing a significant increment of the cost function are extracted among the δ's uncertainty instances. The same issue arises in the 4D footprint calculation as illustrated graphically in Figure 2.3.
To avoid this problem, it would be useful to have a simple procedure for discarding such extractions without affecting the guarantees provided by Theorem 1. In [14], a variant of the scenario method that includes constraint removal is proposed and feasibility of the obtained solution is proven. The associated scenario program is as follows

$$\min_{A,\boldsymbol{c}} \ \log\det A^{-1} \tag{2.3.6}$$

subject to: $A = A^T \succ 0$

$$(\boldsymbol{x}_{\delta^{(i)}}(t)-\boldsymbol{c})^T A\,(\boldsymbol{x}_{\delta^{(i)}}(t)-\boldsymbol{c}) \leq 1,\ i \in \{1,2,\ldots,N\} \setminus \{i_1,\ldots,i_k\},$$

where $\{i_1,\ldots,i_k\} \subset \{1,2,\ldots,N\}$ are the indices of the uncertainty instances that are removed so as to improve the cost (i.e. reduce the volume of the ellipsoid).

Theorem 2. *Select a "violation parameter" $\varepsilon \in (0,1)$, a "confidence parameter9' $\eta \in (0,1)$ and an "empirical violation parameter" $\alpha \in [0,\epsilon)$. If N is such that*

$$\binom{\lfloor \alpha N \rfloor + d}{\lfloor \alpha N \rfloor} \sum_{i=0}^{\lfloor \alpha N \rfloor + d} \binom{N}{i} \varepsilon^i (1-\varepsilon)^{N-i} \leq \eta, \tag{2.3.7}$$

where d denotes the number of optimization variables in (2.3.3), then, if we set $k = \lfloor \alpha N \rfloor$, the solution $(A^\star_{N,k}, \boldsymbol{c}^\star_{N,k})$ to the scenario optimiza-

tion problem with constraint removal (2.3.6) *satisfies*

$$\mathcal{P}\left\{\delta \in \Delta:\ \left(\boldsymbol{x}_\delta(t) - \boldsymbol{c}^\star_{N,k}\right)^T A^\star_{N,k}\left(\boldsymbol{x}_\delta(t) - \boldsymbol{c}^\star_{N,k}\right) \leq 1\right\} \geq 1 - \varepsilon,$$

with probability no smaller than $1 - \eta$.

Remark 2 (Choice of the empirical probability of violation α). The empirical probability of violation α is an user-chosen parameter through which the level of approximation of the randomized solution can be tuned. If one chooses $\alpha = 0$, then, no constraints are removed and the problem reduces to finding a solution to a single constrained optimization problem. This is computationally attractive, but the actual violation of the obtained randomized solution is typically much smaller than the desired ε and the ellipsoid much larger than needed. As a matter of fact, though the feasibility of the randomized solution is guaranteed for every $\alpha \in [0, \varepsilon)$, it is intuitively clear that the closer α to the desired violation probability ε the better the randomized solution approximates the actual solution to the chance-constrained problem. At the same time, however, N grows to infinity as $O(\frac{1}{\varepsilon-\alpha})$ when $\alpha \to \varepsilon$, [14]. □

The optimal removal procedure is computationally impracticable, but since Theorem 2 holds irrespectively of the algorithm used to remove the constraints, one can head for suboptimal approaches like removing one by one the constraint that leads to the largest improvement in the cost (greedy removal) or subsequently removing the whole set of active constraints (block removal). Algorithm 1 implements this latter removal rule for 3D footprint calculation. The shorthand $\boldsymbol{x}_t^{(i)}$ is adopted for $\boldsymbol{x}_{\delta^{(i)}}(t)$ for ease of notation. Note that in step 6.5 of Algorithm 1, the number of constraints that are violated by the current solution is evaluated. Indeed, discarded constraints may become active at some subsequent removal step and for the result in Theorem 2 to hold, exactly k constraints have to be violated by the solution $(A^\star_{N,k}, \boldsymbol{c}^\star_{N,k})$.

Algorithm 1 3D randomized footprint

INPUT ε AND α AND η

SET N AND k according to Theorem 2

FOR $i := 1$ TO N

  SET $\delta^{(i)}$:= random extraction from Δ according to $\mathcal{P}$

  SET $\boldsymbol{x}_t^{(i)}$:= solution to (2.2.1) at time t when the uncertain elements are equal to $\delta^{(i)}$

END FOR

SET $\{A^\star, \boldsymbol{c}^\star\} := \arg\min \log\det A^{-1}$

subject to: $A = A^T \succ 0$,

$$\left(\boldsymbol{x}_t^{(i)} - \boldsymbol{c}\right)^T A \left(\boldsymbol{x}_t^{(i)} - \boldsymbol{c}\right) \leq 1, i = 1, \ldots, N;$$

SET $V := \emptyset$ AND $p := 0$;

% V is the set of indexes of constraints violated by $\{A^\star, \boldsymbol{c}^\star\}$

% p is the cardinality of V

WHILE $p < k$

  SET $\{i_1, i_2, \ldots, i_m\} := \left\{i : \left(\boldsymbol{x}_t^{(i)} - \boldsymbol{c}^\star\right)^T A^\star \left(\boldsymbol{x}_t^{(i)} - \boldsymbol{c}^\star\right) = 1\right\}$;

  % $\{i_1, i_2, \ldots, i_m\}$ are the indexes of active constraints

  IF $m > k - p$

    SET $\{j_1, j_2, \ldots, j_{k-p}\} := k - p$ random integers extracted from $\{1, 2, \ldots, m\}$ without repetition

    SET $R := \{i_{j_1}, i_{j_2}, \ldots, i_{j_{k-p}}\} \subset \{i_1, i_2, \ldots, i_m\}$

  ELSE

    SET $R := \{i_1, i_2, \ldots, i_m\}$

  END IF

  % R is the set of indexes of constraints to be removed

  SET $\{A^\star, \boldsymbol{c}^\star\} := \arg\min \log\det A^{-1}$

  subject to: $A = A^T \succ 0$,

$$\left(\boldsymbol{x}_t^{(i)} - \boldsymbol{c}\right)^T A \left(\boldsymbol{x}_t^{(i)} - \boldsymbol{c}\right) \leq 1, i \in \{1, 2, \ldots, N\} \setminus (R \cup V);$$

  SET $V := \left\{i : \left(\boldsymbol{x}_t^{(i)} - \boldsymbol{c}^\star\right)^T A^\star \left(\boldsymbol{x}_t^{(i)} - \boldsymbol{c}^\star\right) > 1\right\}$ AND $p := |V|$;

  % V is the set of indexes of constraints violated by $\{A^\star, \boldsymbol{c}^\star\}$

  % p is the cardinality of V

END WHILE

RETURN $\{A^\star, \boldsymbol{c}^\star\}$.

4D debris footprint

In order to extend the characterization of the debris dispersion to 4D, we need to account also for time. This would naturally lead to the following chance-constrained optimization:

$$\begin{aligned} \min_{(A_t,\boldsymbol{c}_t),t\in[t_i,t_f]} \quad & \int_{t_i}^{t_f} \log\det A_t^{-1} dt \\ \text{subject to:} \quad & A_t = A_t^T \succ 0,\ t \in [t_i, t_f] \\ & \mathcal{P}\Big\{\delta \in \Delta :\ \max_{t\in[t_i,t_f]} \left(\boldsymbol{x}_\delta(t) - \boldsymbol{c}_t\right)^T A_t \left(\boldsymbol{x}_\delta(t) - \boldsymbol{c}_t\right) \leq 1\Big\} \geq 1-\varepsilon, \end{aligned} \tag{2.3.8}$$

where $[t_i, t_f]$ is the reference time horizon when the debris is falling, and to the 4D footprint description as

$$\mathcal{E}_\varepsilon^\star(t) = \{\boldsymbol{x} \in \Re^3 :\ \left(\boldsymbol{x} - \boldsymbol{c}_t^\star\right)^T A_t^\star \left(\boldsymbol{x} - \boldsymbol{c}_t^\star\right) \leq 1\},\ t \in [t_i, t_f],$$

with $(A_t^\star, c_t^\star)$, $t \in [t_i, t_f]$, denoting the solution to (2.3.8).
Unfortunately, the 4D chance-constrained problem (2.3.8) is even more challenging to solve than its 3D counterpart (2.3.2), given that the optimization variables $(A_t, \boldsymbol{c}_t)$ are functions of time $t \in [t_i, t_f]$ and, hence, infinite dimensional. A possible solution to reduce the optimization variables to a finite number is to finitely parameterized A_t and $\boldsymbol{c}_t$ as a function of time. Alternatively, one can discretize time and associate to each sample time instant an ellipsoid. The sum of the volumes of all ellipsoids is then minimized subject to the constraint that a fraction of probability at least $1-\varepsilon$ of the debris trajectories belongs to the ellipsoids. We opt for this latter option.
Let t_j, $j = 1, \ldots, n_s$, be the sampled time instants along the reference time horizon $[t_i, t_f]$, and A_j and $\boldsymbol{c}_j$ the parameters of the ellipsoid associated with time t_j. Then, we have:

$$\begin{aligned} \min_{(A_j,\boldsymbol{c}_j),j=1,\ldots,n_s} \quad & \sum_{k=1}^{n_s} \log\det A_j^{-1} \\ \text{subject to:} \quad & A_j = A_j^T \succ 0,\ j = 1, \ldots, n_s \\ & \mathcal{P}\Big\{\delta \in \Delta :\ \max_{j=1,\ldots,n_s} \left(\boldsymbol{x}_\delta(t_j) - \boldsymbol{c}_j\right)^T A_j \left(\boldsymbol{x}_\delta(t_j) - \boldsymbol{c}_j\right) \leq 1\Big\} \geq 1-\varepsilon, \end{aligned} \tag{2.3.9}$$

a chance-constrained optimization problem which can be solved via scenario approach with constraint removal. The resulting algorithm is described next.

Algorithm 2 4D randomized footprint

INPUT ε AND α AND η AND $\{t_j\}_{j=1,\dots,n_s}$

SET N AND k according to Theorem 2

FOR $i := 1$ TO N

  SET $\delta^{(i)}$:= random extraction from Δ according to $\mathcal{P}$

  SET $\boldsymbol{x}_{t_j}^{(i)}$:= solution to (2.2.1) at time t_j when the uncertain elements are equal to $\delta^{(i)}$, with $j = 1, \dots, n_s$

END FOR

SET $\{A_j^\star, \boldsymbol{c}_j^\star\}_{j=1,\dots,n_s} := \arg\min \sum_{k=1}^{n_s} \log\det A_j^{-1}$

subject to: $A_j = A_j^T \succ 0,\ j = 1, \dots, n_s;$

$$\max_{j=1,\dots,n_s} (\boldsymbol{x}_{t_j}^{(i)} - \boldsymbol{c}_j)^T A_j (\boldsymbol{x}_{t_j}^{(i)} - \boldsymbol{c}_j) \le 1, i = 1, \dots, N;$$

SET $V := \emptyset$ AND $p := 0$;

% V is the set of indexes of constraints violated by $\{A_j^\star, \boldsymbol{c}_j^\star\}_{j=1,\dots,n_s}$

% p is the cardinality of V

WHILE $p < k$

  SET $\{i_1, i_2, \dots, i_m\} := \left\{ i : \max_{j=1,\dots,n_s} (\boldsymbol{x}_{t_j}^{(i)} - \boldsymbol{c}_j^\star)^T A_j^\star (\boldsymbol{x}_{t_j}^{(i)} - \boldsymbol{c}_j^\star) = 1 \right\}$;

  % $\{i_1, i_2, \dots, i_m\}$ are the indexes of active constraints

  IF $m > k - p$

    SET $\{j_1, j_2, \dots, j_{k-p}\} := k - p$ random integers extracted from $\{1, 2, \dots, m\}$ without repetition

    SET $R := \{i_{j_1}, i_{j_2}, \dots, i_{j_{k-p}}\} \subset \{i_1, i_2, \dots, i_m\}$

  ELSE

    SET $R := \{i_1, i_2, \dots, i_m\}$

  END IF

  % R is the set of indexes of constraints to be removed

  SET $\{A_j^\star, \boldsymbol{c}_j^\star\}_{j=1,\dots,n_s} := \arg\min \sum_{k=1}^{n_s} \log\det A_j^{-1}$

  subject to: $A_j = A_j^T \succ 0,\ j = 1, \dots, n_s;$

  $$\max_{j=1,\dots,n_s} (\boldsymbol{x}_{t_j}^{(i)} - \boldsymbol{c}_j)^T A_j (\boldsymbol{x}_{t_j}^{(i)} - \boldsymbol{c}_j) \le 1, i \in \{1, 2, \dots, N\} \setminus (R \cup V);$$

  SET $V := \left\{ i : \max_{j=1,\dots,n_s} (\boldsymbol{x}_{t_j}^{(i)} - \boldsymbol{c}_j^\star)^T A_j^\star (\boldsymbol{x}_{t_j}^{(i)} - \boldsymbol{c}_j^\star) > 1 \right\}$ AND $p := |V|$;

  % V is the set of indexes of constraints violated by $\{A_j^\star, \boldsymbol{c}_j^\star\}_{j=1,\dots,n_s}$

  % p is the cardinality of V

END WHILE

RETURN $\{A_j^\star, \boldsymbol{c}_j^\star\}_{j=1,\dots,n_s}$.

It is worth noticing that the optimization problems at steps 4 and 6.4 can actually be decoupled in n_s optimization problems, and, hence, the n_s minimum volume ellipsoids associated with the time instants t_j, $j = 1, \ldots, n_s$, can be determined separately, according to the same procedure described in the 3D footprint section. The coupling element in the overall optimization procedure is in fact the constraint removal.

2.3.2 Covariance propagation method

In this section we briefly recall the *covariance propagation method* proposed in [39] for determining the 4D footprint. This approach rests on the linearization of the debris equations (2.2.1) around the nominal trajectory and on the description of the resulting perturbation as a Gauss-Markov process. Dispersion around the nominal trajectory can then be quantified through the ellipsoids representing the level curves of the Gaussian probability density function characterizing the Gauss-Markov process.
Set $\boldsymbol{s} = [\boldsymbol{x}^T, \boldsymbol{v}^T]^T$. Then, equations (2.2.1) can be rewritten in the compact form

$$\dot{\boldsymbol{s}} = \boldsymbol{f}(\boldsymbol{s}) + B\boldsymbol{\xi},$$

where $B = [0_{3\times3}\ I_{3\times3}]^T$.
Now, define the perturbation vector $\boldsymbol{z}$ as

$$\boldsymbol{z} = \boldsymbol{s} - \boldsymbol{s}_n,$$

where $\boldsymbol{s}_n$ is the nominal trajectory obtained by neglecting $\boldsymbol{\xi}$ and the other sources of uncertainty affecting the system evolution. If we assume that the wind velocity vector $\boldsymbol{w}$ entering the equations (2.2.1) through the atmospheric drag deceleration (2.2.3) depends on the position only (i.e., $\boldsymbol{w} = \boldsymbol{w}(\boldsymbol{x})$), then, the linearized equations governing $\boldsymbol{z}$ are given by

$$\dot{\boldsymbol{z}} = A(t)\,\boldsymbol{z} + B\boldsymbol{\xi}, \tag{2.3.10}$$

with

$$A(t) = \left.\frac{\partial \boldsymbol{f}}{\partial \boldsymbol{s}}\right|_{\boldsymbol{s}_n(t)} = \begin{bmatrix} 0_{3\times3} & I_{3\times3} \\ F(\boldsymbol{s}_n) + F_e & G(\boldsymbol{s}_n) + G_e \end{bmatrix},$$

where

$$F_e = \begin{bmatrix} \omega_e^2 & 0 & 0 \\ 0 & \omega_e^2 \sin^2 \varphi_0 & -\omega_e^2 \sin \varphi_0 \cos \varphi_0 \\ 0 & -\omega_e^2 \sin \varphi_0 \cos \varphi_0 & \omega_e^2 \cos^2 \varphi_0 \end{bmatrix},$$

$$G_e = \begin{bmatrix} 0 & 2\omega_e \sin \varphi_0 & -2\omega_e \cos \varphi_0 \\ -2\omega_e \sin \varphi_0 & 0 & 0 \\ 2\omega_e \cos \varphi_0 & 0 & 0 \end{bmatrix},$$

and $F(\cdot)$ and $G(\cdot)$ are 3×3 matrix whose elements (i, j) are given by

$$F_{i,j}(\boldsymbol{s}) = \frac{1}{2\beta} \left[\rho \left(\frac{v_{r_i}}{v_r} \boldsymbol{v}_r^T \frac{\partial \boldsymbol{w}}{\partial x_j} + v_r \frac{\partial w_i}{\partial x_j} \right) - \frac{\partial \rho}{\partial x_j} v_r v_{r_i} \right],$$

$$G_{i,j}(\boldsymbol{s}) = \begin{cases} -\dfrac{\rho}{2\beta} \left[\dfrac{v_{r_i} v_{r_j} + v_r^2}{v_r} \right], & \text{if } i = j \\ \\ -\dfrac{\rho}{2\beta} \left[\dfrac{v_{r_i} v_{r_j}}{v_r} \right], & \text{if } i \neq j. \end{cases}$$

Suppose that the disturbance vector $\boldsymbol{\xi}$ is a white Gaussian noise with mean and covariance

$$E[\boldsymbol{\xi}(t)] = \overline{\boldsymbol{\xi}}(t) \quad \text{and} \quad E\left[\left(\boldsymbol{\xi}(t) - \overline{\boldsymbol{\xi}}(t) \right) \left(\boldsymbol{\xi}(t) - \overline{\boldsymbol{\xi}}(t) \right)^T \right] = \Xi(t),$$

and it is independent of the initial condition $\boldsymbol{z}(0)$. If $\boldsymbol{z}(0)$ is Gaussian $\boldsymbol{z}(0) \sim \mathcal{N}(\overline{\boldsymbol{z}}_0, Z_0)$, then, equation (2.3.10) describes a continuous time Gauss-Markov process with mean $\overline{\boldsymbol{z}}(t) = E[\boldsymbol{z}(t)]$ and covariance matrix
$Z(t) = E\left[(\boldsymbol{z}(t) - \overline{\boldsymbol{z}}(t)) (\boldsymbol{z}(t) - \overline{\boldsymbol{z}}(t))^T \right]$ satisfying the following equations:

$$\begin{aligned} \dot{\overline{\boldsymbol{z}}} &= A(t) \overline{\boldsymbol{z}} + B \overline{\boldsymbol{\xi}}(t) \\ \dot{Z} &= A(t) Z + Z A(t) + B \Xi(t) B^T \end{aligned} \tag{2.3.11}$$

initialized with $\overline{\boldsymbol{z}}(0) = \boldsymbol{z}_0$ and $Z(0) = Z_0$.
The debris position at time t can then be described as a Gaussian random

variable with mean and covariance matrix

$$\overline{\boldsymbol{x}}(t) = C(\overline{\boldsymbol{z}}(t) + s_n(t))$$
$$X(t) = CZ(t)C^T$$

where $C = [I_{3\times 3}\ 0_{3\times 3}]$.
As a consequence, the 3D ellipsoid containing a fraction $1-\varepsilon$ of the debris trajectories at time t can be determined as an appropriate level set of the Gaussian distribution of $\overline{\boldsymbol{x}}(t)$, i.e.,

$$\mathcal{E}_\varepsilon(t) := \{x \in \Re^3 : [\boldsymbol{x} - \overline{\boldsymbol{x}}(t)]^T X^{-1}(t)[\boldsymbol{x} - \overline{\boldsymbol{x}}(t)] \leq r_\varepsilon^2\}, \tag{2.3.12}$$

where r_ε is the Mahalanobis distance between $\boldsymbol{x}$ and $\overline{\boldsymbol{x}}$ and can be computed as the $1-\varepsilon$ quantile of the χ^2 distribution with 3 degrees of freedom:

$$\mathcal{P}(V \leq r_\varepsilon^2) = 1-\varepsilon \qquad \text{with } V \sim \chi^2(3).$$

The 4D footprint can then be obtained by varying t within the reference time horizon $[t_i, t_f]$ and considering the corresponding ellipsoidal set $\mathcal{E}_\varepsilon(t)$, $t \in [t_i, t_f]$. Note that here $t_i = 0$.

Remark 3 (approximation errors in the covariance propagation method). It is worth noticing that there are two sources of approximation in the evaluation of the 4D footprint according to the outlined procedure: 1) the footprint is constructed based on a linearized model of the system and 2), even if the linearized model were the actual system, there is no guarantee that a fraction of probability $1-\varepsilon$ of the trajectories passes through *all* the ellipsoidal sets $\mathcal{E}(t)$, $t \in [t_i, t_f]$. □

2.3.3 Comparative analysis

In order to compare the Simulation-Based (SB) method in Section 2.3.1 with the Covariance Propagation (CP) method in Section 2.3.2, we suppose that the only source of uncertainty is the initial state $\boldsymbol{s}(0)$ and consider the disturbance vector $\boldsymbol{\xi}(t)$ in (2.2.1) negligible, as in the simulation results presented in [39]. Differently from the simulation setting in [39], we used HWM93 instead of HWM07 as nominal local wind model [18] and we adopted the U.S. Standard Atmosphere [1, 2] instead of the MSISE-00 model to obtain atmospheric density in the range 0 to 120 km.

Results reported in this section refer to the case when the initial state $\boldsymbol{s}(0)$ is given by

$$\boldsymbol{s}(0) = \boldsymbol{s}_n(0) + \boldsymbol{z}(0),$$

where the nominal initial state is $\boldsymbol{s}_n(0) = [\boldsymbol{x}_n(0)^T, \boldsymbol{v}_n(0)^T]^T$, with $\boldsymbol{x}_n(0) = [0, 0, 7.8 \cdot 10^4]^T$ m and $\boldsymbol{v}_n(0) = [7.0989 \cdot 10^3, 0, -123.9]^T$ m/s and the perturbation to the nominal initial state $\boldsymbol{z}(0)$ is Gaussian with mean $\overline{\boldsymbol{z}}_0 = 0$ and covariance matrix

$$Z_0 = \begin{bmatrix} 0_{3\times 3} & 0_{3\times 3} \\ 0_{3\times 3} & V_0 \end{bmatrix}.$$

where

$$V_0 = \begin{bmatrix} \sigma^2_{v_x} & 0 & 0 \\ 0 & \sigma^2_{v_y} & 0 \\ 0 & 0 & \sigma^2_{v_z} \end{bmatrix}, \tag{2.3.13}$$

where $\sigma^2_{v_x} = \sigma^2_{v_y} = 2500$ m^2/s^2 and $\sigma^2_{v_z} = 5300$ m^2/s^2.
Thus, the initial position $\boldsymbol{x}(0)$ of the reentering object is assumed to be known, whereas the initial velocity $\boldsymbol{v}(0)$ is uncertain.
Computation of the 4D footprint according to the simulation-based method implemented in Algorithm 2 involves integrating N times the debris dynamics in (2.2.1) starting from N sampled values for $\boldsymbol{s}(0)$ extracted from the Gaussian distribution with mean $\boldsymbol{s}_n(0)$ and variance Z_0.
The time instants $\{t_j\}_{j=1,\dots,n_s}$ for the 4D footprint calculation are determined by considering $n_s = 10$ equally spaced samples of the nominal trajectory along the the z axis (i.e. the altitude in the ENZ reference frame). The ellipsoids associated to $\{t_j\}_{j=1,\dots,n_s}$ are then computed based on the positions of the debris along the N simulated trajectories at the corresponding time instant.
Different values for the violation parameter ε and for the empirical violation α (chosen so as to assure a reasonable computational burden, see Remark 2) are considered, whereas the confidence parameter η is set equal to $\eta = 10^{-5}$ in all runs of Algorithm 2. The value for N satisfying the bound in Theorem 2 depend on the considered $(\varepsilon, \alpha, \eta)$, the maximal N being $N = 10780$.
Computation of the 4D footprint according to the covariance propagation method rests on determining the 3D ellipsoidal sets in (2.3.12) at the sample times $\{t_j\}_{j=1,\dots,10}$ through the solution to (2.3.11).
Table 2.1 summarizes the results obtained with the SB method and the CP

method for a set of values of ε. The value for α used in the SB method is specified in the second column. In all runs of Algorithm 2 we maintain fixed $N = 10780$ and remove $k = \lfloor \alpha N \rfloor$ constraints.
The comparison between the SB method and CP method is in terms of i) volume of the corresponding 4D footprints (reported in km^3 in the last two columns of Table 2.1) and ii) actual violation $\hat{\varepsilon}$ computed via Monte Carlo simulation by generating a further set of N simulated trajectories and evaluating the fraction of them that exits the 4D footprint.

ε	α	$\hat{\varepsilon}_N^{SB}$	$\hat{\varepsilon}_N^{CP}$	V^{SB}	V^{CP}
0.500	0.350	0.3505	0.5933	452.47	235.10
0.400	0.260	0.2602	0.5083	625.91	326.69
0.300	0.170	0.1705	0.4261	907.73	453.24
0.200	0.100	0.1003	0.3366	1304.18	646.03
0.100	0.035	0.0353	0.2370	2208.56	1009.74
0.050	0.010	0.0103	0.1724	3552.52	1411.29
0.025	0.002	0.0020	0.1328	5494.42	1846.50
0.020	0.001	0.0012	0.1224	6845.50	1993.27
0.015	0	$< 5 \cdot 10^{-5}$	0.1109	9182.69	2187.03

Table 2.1: Comparative analysis of the two methods.

Note that if we look at each single row of Table 2.1, the 4D footprint volume V^{SB} obtained with the SB method is larger than volume V^{CP} obtained with the CP method (see also Figure 2.1 corresponding to $\varepsilon = 0.30$ for a pictorial view). However, the violation $\hat{\varepsilon}^{CP}$ of the CP method always exceeds the desired ε value (possibly due to the approximations errors involved in the method, see Remark 3), whereas the violation $\hat{\varepsilon}^{SB}$ of the SB method is always smaller, so that if we compare the volume of the 4D footprints having the same violation (i.e., $\hat{\varepsilon}^{CP} \simeq \hat{\varepsilon}^{SB}$), the SB method outperforms the CP one. For instance, if we consider the third and sixth rows, $\hat{\varepsilon}^{SB} = 0.1705$ and $V^{SB} = 907.73$ (third row) and $\hat{\varepsilon}^{CP} = 0.1724 \simeq \hat{\varepsilon}^{SB}$ and $V^{CP} = 1411.29 \gg V^{SB}$ (sixth row). The corresponding footprints are shown in Figure 2.2.
As for the SB method, it is worth noticing that actual violation $\hat{\varepsilon}_N^{SB}$ is very close to the chosen empirical violation α, which affects the size of the 4D footprint. This is better pointed out in Figure 2.3, whose plots refer to the same $\varepsilon = 0.1$ but different α's: $\alpha = 0$ for the plot on the left and $\alpha = 0.035$ for the plot on the right. The debris nominal trajectory is depicted in blue with a solid line, whereas the other simulated trajectories used for

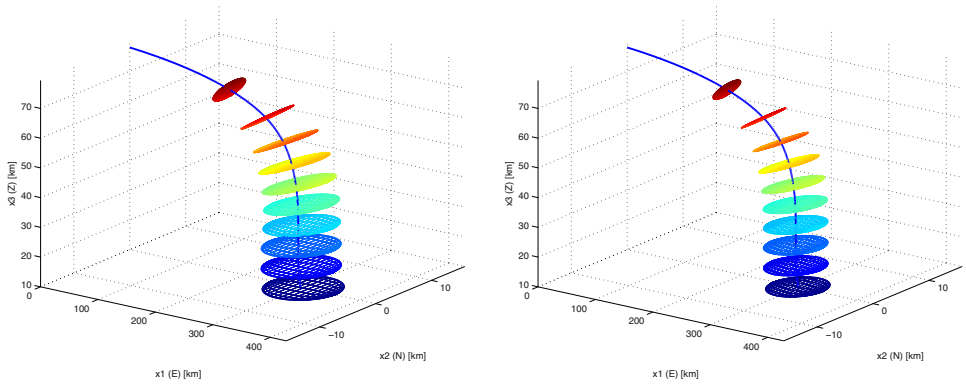

Figure 2.1: 4D footprint: SB method (left) and CP method (right) with $\varepsilon = 0.30$

the footprint constructions are dotted, reporting their samples at the time instants $\{t_j\}_{j=1,\dots,n_s}$. In the plot on the left, corresponding to no constraint removal ($\alpha = 0$), all simulated trajectories belong to the 4D footprint and are represented through cyan dots; in the plot on the right, some of the simulated trajectories do not belong to the 4D footprint and are represented through red dots. These red dotted trajectories actually correspond to those constraints that have been removed and are violated by the solution to Algorithm 2 with $\alpha = 0.035$. Clearly, considering all simulated trajectories leads to an overestimation of the 4D footprint corresponding to $\varepsilon = 0.1$.
Besides its improved performance with respect to the CP method, the SB method is also applicable to a more general setting, where other sources of uncertainties are present besides that on the initial velocity. As a matter of

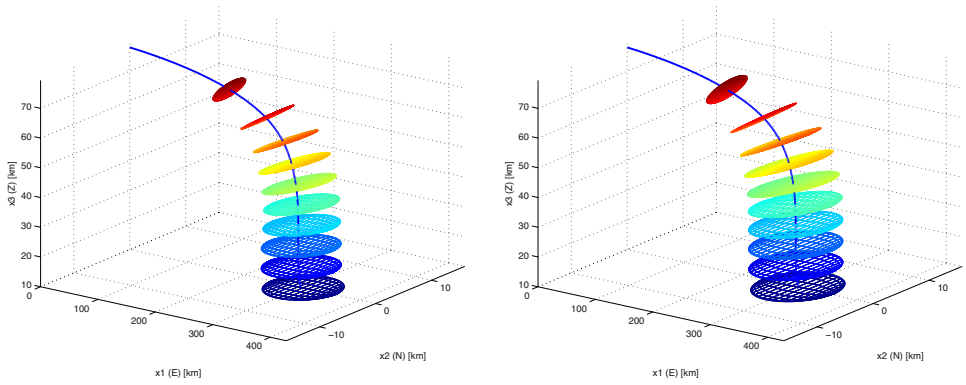

Figure 2.2: 4D footprint: SB method (left) with $\varepsilon = 0.30$ and CP method (right) with $\varepsilon = 0.05$

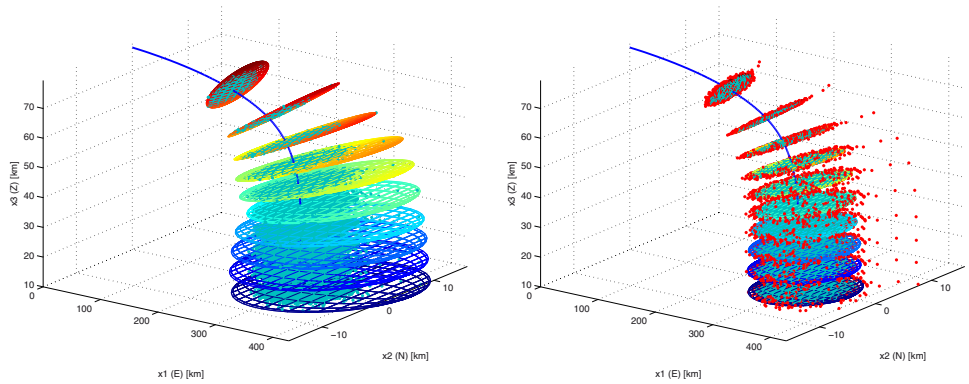

Figure 2.3: 4D footprint: simulation-based approach with $\varepsilon = 0.1$. Plot on the left: $\alpha = 0$. Plot on the right: $\alpha = 0.035$

fact, the approach in [39] is not applicable to the case when other sources of uncertainty (like that on the ballistic coefficient or the local wind) are present, and the authors mention this limit in their final remarks.
Table 2.2 reports the results obtained with the SB method, when a random wind field generated according to [38, 26] (see Section 3.2.3 for more details) is added to the forecasted HWM93 wind at altitudes in the range of 10 to 12 kilometers. In particular, the volumes of the 3D footprint at altitude 10 km obtained with and without the stochastic wind are compared, showing (not surprisingly) a significant increase in the former case.

ε	$V_{10\text{km}}^{HWM93}$	$V_{10\text{km}}^{stochastic}$	$\Delta_{\%}$
0.500	5.9016	8.6171	+46.01%
0.400	8.7010	11.9532	+33.24%
0.300	13.1650	16.8500	+27.99%
0.200	20.8521	24.8829	+19.33%
0.100	38.9874	43.7979	+12.34%
0.050	63.5528	80.0239	+25.92%
0.025	115.7958	166.2697	+43.59%
0.020	132.8127	176.6225	+32.99%
0.015	201.3618	238.5551	+18.47%

Table 2.2: SB method: effect on the 3D footprint volume of the stochastic wind introduction.

2.3.4 Risk estimate based on the probabilistic footprint

In this section, we show how the probabilistic footprint can be used to provide a (conservative) estimate of the probability that the debris will enter some protection zone surrounding an aircraft during its reentry in the time interval $T = [t_i, t_f]$. For ease of reference, we shall refer to this event as a *conflict* and use the shorthand notation $\mathcal{C}$.
Given $\varepsilon \in (0,1)$, let $\mathcal{E}_\varepsilon : T \to 2^{\mathbb{R}^3}$ denote the set-valued map that provides for each time $t \in T$ the corresponding 3D footprint of the debris with violation ε, i.e., the region $\mathcal{E}_\varepsilon(t) \subset \mathbb{R}^3$ occupied by the debris with probability larger than or equal to $1-\varepsilon$. The probability $\mathcal{P}_c$ of a conflict between aircraft i and the space debris in the time horizon T can then be expressed as:

$$\mathcal{P}_c = \mathcal{P}\left(\mathcal{C} \wedge \boldsymbol{x}(t) \in \mathcal{E}_\varepsilon(t)\ \forall t \in T\right) + \mathcal{P}\left(\mathcal{C} \wedge \boldsymbol{x}(t) \notin \mathcal{E}_\varepsilon(t) \text{ for some } t \in T\right)$$

where $\boldsymbol{x}(t)$ denotes the debris position at time $t \in T$.
By the definition of $\mathcal{E}_\varepsilon$, the second term in the right-end-side can be upper bounded as follows:

$$\mathcal{P}\left(\mathcal{C} \wedge \boldsymbol{x}(t) \notin \mathcal{E}_\varepsilon(t) \text{ for some } t \in T\right) \leq \mathcal{P}\left(\boldsymbol{x}(t) \notin \mathcal{E}_\varepsilon(t) \text{ for some } t \in T\right) \leq \varepsilon$$

The first term in the right-end-side can be upper bounded as follows:

$$\begin{aligned}
&\mathcal{P}\left(\mathcal{C} \wedge \boldsymbol{x}(t) \in \mathcal{E}_\varepsilon(t)\ \forall t \in T\right) \\
&= \mathcal{P}\left(\mathcal{C} \wedge \boldsymbol{x}_i(t) \in \mathcal{E}_\varepsilon(t) \text{ for some } t \in T \wedge \boldsymbol{x}(t) \in \mathcal{E}_\varepsilon(t)\ \forall t \in T\right) \\
&\leq \mathcal{P}\left(\boldsymbol{x}_i(t) \in \mathcal{E}_\varepsilon(t) \text{ for some } t \in T \wedge \boldsymbol{x}(t) \in \mathcal{E}_\varepsilon(t)\ \forall t \in T\right) \\
&\leq \min\left\{\mathcal{P}\left(\boldsymbol{x}_i(t) \in \mathcal{E}_\varepsilon(t) \text{ for some } t \in T\right), \mathcal{P}\left(\boldsymbol{x}(t) \in \mathcal{E}_\varepsilon(t)\ \forall t \in T\right)\right\} \\
&\leq \min\left\{\mathcal{P}\left(\boldsymbol{x}_i(t) \in \mathcal{E}_\varepsilon(t) \text{ for some } t \in T\right), 1-\varepsilon\right\},
\end{aligned}$$

where $\boldsymbol{x}_i$ denotes the position of aircraft i.
As a result:

$$\mathcal{P}_c \leq \varepsilon + \min\left\{\mathcal{P}\left(\boldsymbol{x}_i(t) \in \mathcal{E}_\varepsilon(t) \text{ for some } t \in T\right), 1-\varepsilon\right\} \tag{2.3.14}$$

The problem is then estimating the probability that aircraft i will enter $\mathcal{E}_\varepsilon$ within T:

$$\mathcal{P}\left(\boldsymbol{x}_i(t) \in \mathcal{E}_\varepsilon(t) \text{ for some } t \in T\right),$$

which can be done via Monte Carlo simulations.
The level of conservativeness of the obtained upper bound (2.3.14) obviously depends on the volume of the footprint. In the next chapter, we shall present an approach to reduce the footprint size by exploiting the measurements of the aircraft and debris positions. This is achieved by combining the proposed simulation-based approach with nonlinear filtering techniques.
A bound similar to (2.3.14) can be easily derived for the probability of conflict between the debris and at least one of the aircraft flying in the airspace region involved in the debris reentry.

Chapter 3

Prediction of no-fly zones for air traffic

3.1 Introduction

In this chapter, we address the problem of using available measurements on debris and aircraft positions so as to reduce the uncertainty affecting the reentering debris dispersion and improve its probabilistic footprint estimation. This should result in the identification of smaller no-fly zones for the aircraft, and, hence, facilitate the air traffic controllers' task of making the aircraft avoid hazard areas and safely arrive at their destination.
The proposed approach involves the adoption of nonlinear filtering techniques and their integration in the footprint calculation. The idea is to use the Particle Filter so as to gather information from the aircraft radar measurements on the actual wind field (i.e. reduce wind forecast errors), and to run simultaneously the Unscented Kalman Filter so as to determine the a-posteriori probability of the debris state given also the measurements of its position.
We shall first introduce air traffic modeling, presenting single aircraft dynamics, the flight management system, and a model for characterizing wind forecasts errors. We adopt a stochastic linear system to emulate wind evolution in the region of interest of the airspace, as suggested in [26]. After that, we deploy the most famous implementation of the Bayesian recursive estimation, the Particle Filter, and basically use aircraft as sensors to reduce the uncertainty on the actual wind.

Then, later on in the chapter, we show how the Unscented Kalman Filter, an extension of the regular Kalman filter to address nonlinear estimation, can be used to filter the debris observations in order to reduce the uncertainty on its dispersion and improve the footprint estimation.
Unfortunately the Particle Filter cannot be applied to both the debris and aircraft radar measurements because of a phenomenon called "sample impoverishment" [41] that occurs when only a few of the particles that jointly represent the a-posteriori probability of the state given the measurements are compatible with the available measurements. Indeed, [41] reports an example in which the Unscented Kalman Filter performs better than the Particle Filter in estimating altitude, velocity, and ballistic coefficient of an object falling on Earth. A similar example is discussed in [24]. Sample impoverishment is instead avoided when applying the Particle Filter to the aircraft measurements because of the ad-hoc implementation described in [26], exploiting the linear dynamics governing the stochastic wind.
In the final part of the chapter we report the results obtained in a simulation example, and compare the footprint estimation method based on joint use of the Unscented Kalman Filtering and Particle Filtering with alternative approaches, namely, the worst-case and best-case ones. The worst-case approach uses only the debris measurements and the Unscented Kalman Filter, whereas the best-case approach is just introduced for comparative purposes and exploits the perfect knowledge of the debris state and the wind field for determining the footprint.

3.2 Air traffic: modeling

In this section we describe the aircraft model that we shall use to carry out wind estimation for footprint reduction. The model was developed in [26, 27, 28] and comprises three main components: the continuous dynamics regarding the physical motion of the aircraft in the airspace, the discrete dynamics determining the Flight Management System (FMS) action, and the stochastic wind component affecting the aircraft motion. As such it is a stochastic hybrid system.

3.2.1 Aircraft continuous model

A point mass model is adopted for an aircraft flying in a 3D airspace. Although it disregards a lot of complicated aspects about flight dynamics this is a good approximation considering the point of view of an air traffic controller.
The model comprises the following variables: X, Y and Z (representing the position of the aircraft based on an inertial reference X_r, Y_r, Z_r with origin fixed on a point on Earth's surface i.e. the radar position), the bank angle (φ), the flight path angle (γ), the heading angle (ψ), the True AirSpeed (V) and the mass (m). All these quantities are drawn in Figure 3.1.

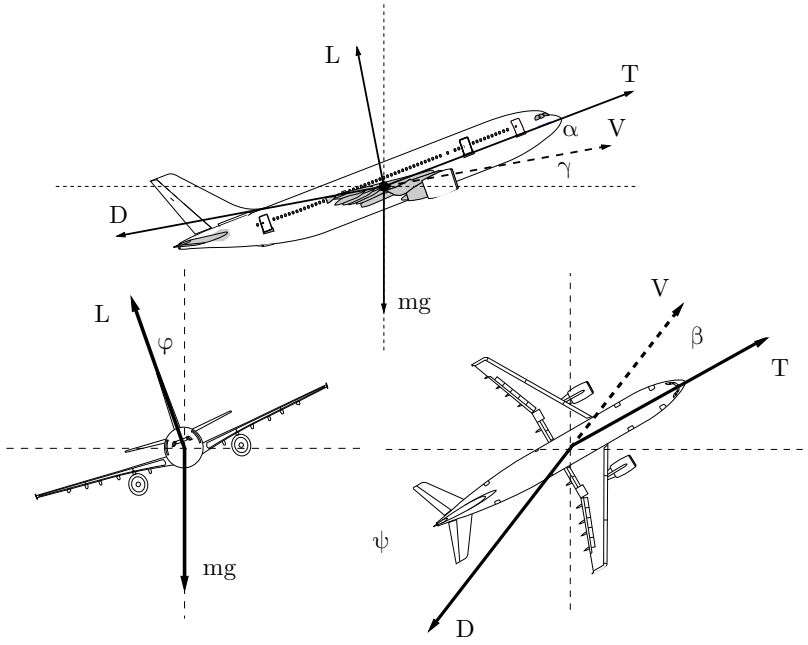

Figure 3.1: Aircraft Dynamics

Regarding the forces acting on the aircraft they are the lift (L) and the drag (D), which depend on the angle of attack (α) and the side slip angle (β). Then we have the engine thrust (T) and the weight (mg). Thrust T affects mass variation through η that represents the fuel consumption. In the equations of motion we must consider also the effect of the wind, acting on the airplane as a disturbance, and entering the aircraft dynamics through its speed $W = (w_x, w_y, w_z) \in \mathbb{R}^3$. The continuous state is composed by X,

Y, Z, V, ψ, m and is governed by the following equations:

$$\begin{bmatrix} \dot{X} \\ \dot{Y} \\ \dot{Z} \\ \dot{V} \\ \dot{\psi} \\ \dot{m} \end{bmatrix} = \begin{bmatrix} Vcos(\psi)cos(\gamma) + w_x \\ Vsin(\psi)cos(\gamma) + w_y \\ Vsin(\gamma) + w_z \\ \dfrac{T - D - mgsin(\gamma)}{m} - W_{agf}cos(\gamma)Vsin(\gamma) \\ \dfrac{1}{m}\dfrac{Lsin(\varphi)}{Vcos(\gamma)} - W_{cgf}tan(\gamma) \\ -\eta T \end{bmatrix} \tag{3.2.1}$$

where

$$W_{agf} = \frac{\partial w_x}{\partial Z}cos(\psi) + \frac{\partial w_y}{\partial Z}sin(\psi)$$

$$W_{cgf} = \frac{\partial w_x}{\partial Z}sin(\psi) + \frac{\partial w_y}{\partial Z}cos(\psi)$$

are the along-track and cross-track wind gradient factors.
Finally considering the system structure and the behaviour of a real aircraft, by ignoring fast dynamics, we can consider T, γ and φ as inputs (i.e. command from pilot for directing the aircraft). Obviously there could be some constraints on the parameters entering the dynamics, which depend on the type of aircraft considered. These kinds of limitations can be retrieved from BADA documents [15].

3.2.2 Flight Management System

The discrete part of the model is related to the Flight Management System (FMS). The aim of the FMS is to collect incoming data from sensors and flight plans (defined through consecutive 3D, or 4D in the latest few years, waypoints) and to set some discrete variables in order to mak ethe aircraft tracking a provided flight plan. The variables used by the FMS are:

- WayPoint index (WP): the index of the waypoint the aircraft is heading towards;
- Acceleration Mode (AM): indicates if the airplane is accelerating, decelerating or cruising;
- Flight Level (FL): the altitude at which the aircraft is flying;
- Climb Mode (CM): indicates if the aircraft is climbing, descending or

flying level;

- Speed Hold Mode (SHM): indicates if the aircraft is holding constant Calibrated AirSpeed (CAS under International Standard Atmosphere conditions is equal to True AirSpeed (TAS)) or constant Mach.

- Flight Phase (FP): distinguishes between Lower Descent, Upper Descent, Approach, Landing;

- Reduced Power Mode (RPM): allows to climb without using all the thrust;

- Troposhpere Mode (TrP): indicates if the aircraft is flying above or below the tropopause (the edge between troposphere and stratosphere).

3.2.3 Wind model

The last component of the aircraft model is the stochastic one and concerns the model of the wind acting on the aircraft. The wind is the most significant source of uncertainty for aircraft dynamics. Here we assume the wind field described as composed by two contributions: the weather forecast (the nominal part) and the forecast error (the stochastic part). For the nominal part we refer to the HWM93 wind model described in [18], through which, given the geodetic coordinates (latitude, longitude and altitude) of a point in the Earth's atmosphere (in the altitude range 0-120 km), we can retrieve mean local value of wind speed along the eastward and northward directions. It should be noted that this model do not describe the intensity along the altitude direction.
The stochastic wind field satisfies the following assumptions:

- vertical component of the wind is supposed to be zero (in agreement with the HWM93 wind model);

- since forecasts obtained from HWM93 are considered as mean values, wind stochastic component is represented as a random Gaussian variable $w(t,p) \sim \mathcal{N}(0, R(t,p,t',p'))$;

- wind components in the X (eastward) and Y (northward) directions are independent, so R is diagonal;

- wind field is isotropic (invariant under rotations) so that the diagonal entries of $R(t,p,t',p')$ are identical and equal to $r(t,p,t',p')$;

- wind variance is constant for all altitudes.

Given these assumptions the covariance matrix R simplifies to

$$R(t,p,t',p') = E\left[w(t,p)w^T(t',p')\right] = \begin{bmatrix} r(t,p,t',p') & 0 \\ 0 & r(t,p,t',p') \end{bmatrix} \quad (3.2.2)$$

where $E[\cdot]$ is the expected value, $p, p' \in \mathbb{R}^3$ and $t, t' \in \mathbb{R}$. Moreover, we have that

$$r(t,p,t',p') = \sigma(Z)\sigma(Z')r_t(|t-t'|)r_{XY}\left(\left\|\begin{matrix} X-X' \\ Y-Y' \end{matrix}\right\|\right) r_Z\left(|AP(Z)-AP(Z')|\right)$$

where $AP(Z)$ is the atmospheric pressure determined using the HWM93 model and $\sigma(Z)$ is the standard deviation of the wind at altitude Z. Quantities $\sigma(Z)$, r_t, r_{XY} and r_Z are defined (and parameters are set) according to [38]:

$$\begin{aligned} r_{XY}(s) &= c_{xy} + (1-c_{xy})e^{-\frac{s}{G_{xy}}} \\ r_Z(s) &= c_z + (1-c_z)e^{-\frac{s}{G_z}} \\ r_t(s) &= c_t + (1-c_t-d_t)e^{-\frac{s}{G_t}} + d_t cos\left(2\pi\frac{s-e_t}{G_t}\right) \end{aligned}$$

It is easy to understand that correlation decays exponentially with the distance in the horizontal plane, with the pressure difference in the vertical direction and with time separation. Values for the parameters are derived based on [38] and result in a strong time-correlation, a significant but smaller horizontal correlation, and a very weak altitude correlation.
In order to generate wind realizations consistent with the above described structure we discretize the airspace in N_x, N_y and N_z cells (each cell is $dx \times dy \times dz$ corresponding to 60 km $\times$ 60 km $\times$ 1 km) and also in N_t time-steps (dt indicates the time interval). Each point of the grid has associated a 2D vector that represents the wind forecast error along the X and Y directions. Let assume $i \in \{1 \dots N_x\}$, $j \in \{1 \dots N_y\}$, $h \in \{1 \dots N_z\}$ and $k \in \{0 \dots N_t\}$. Thanks to this notation we can express the wind at the time

step $t = kdt$ and grid point $p = (idx, jdy, hdz)$ as a vector:

$$w\left[kdt, \begin{pmatrix} idx \\ jdy \\ hdz \end{pmatrix}\right] = \begin{bmatrix} w_x(k,i,j,h) \\ w_y(k,i,j,h) \end{bmatrix}$$

and then lexicographically order it so as to define two vectors

$$W_x(k) = \begin{bmatrix} w_x(k,1,1,1) \\ \vdots \\ w_x(k,N_x,N_y,N_z) \end{bmatrix} \in \mathbb{R}^{N_x N_y N_z}$$

$$W_y(k) = \begin{bmatrix} w_y(k,1,1,1) \\ \vdots \\ w_y(k,N_x,N_y,N_z) \end{bmatrix} \in \mathbb{R}^{N_x N_y N_z}$$

Naming $\hat{R} \in \mathbb{R}^{N_x N_y N_z \times N_x N_y N_z}$ the covariance matrix of both W_x and W_y (due to the isotropicity), wind realizations are generated according to the following linear equations:

$$\begin{cases} W_x(k+1) = aW_x(k) + Qv_x(k+1) \\ W_y(k+1) = aW_y(k) + Qv_y(k+1) \end{cases} \text{with} \begin{cases} W_x(0) = \hat{Q}v_x(0) \\ W_y(0) = \hat{Q}v_y(0) \end{cases} \tag{3.2.3}$$

where $v_x(k), v_y(k) \in \mathbb{R}^{N_x N_y N_z}$ are standard independent Gaussian random variables, and matrices Q and $\hat{Q}$ are derived by using the Cholesky decomposition of $\hat{R}$ according to

$$\hat{Q}\hat{Q}^T = \hat{R} \quad \text{and} \quad QQ^T = (1-a^2)\hat{R} \quad \text{with} \quad a = e^{-\frac{s}{G_t}}.$$

3.2.4 Radar model

Another source of uncertainty is due to the radar measurement instruments. Obviously, radars can only measure a part of the state of all aircraft flying in the airspace that is, for each aircraft, the position (X, Y, Z). So we create a vector $y(k)$ that comprises all the measurements about aircraft position

currently flying in the considered airspace.

$$y(k) = [y(k,1) \dots y(k,M(k))]^T$$
$$y(k,\ell) = \begin{bmatrix} X(k,\ell) \\ Y(k,\ell) \\ Z(k,\ell) \end{bmatrix}$$

where $M(k)$ is the number of aircrafts flying in the airspace at time istant k. Then, the measurement noise can be een as an additive contribution to aircraft coordinates and modeled as an independent Gaussian random variables with zero mean and variance

$$\sigma_r = \begin{cases} 40\text{m} & d \leq 60 \quad \text{km} \\ 1.35 \cdot 10^{-3} d & d > 60 \quad \text{km} \end{cases}$$

where d is the distance of the aircraft from the radar.

3.2.5 Model simplification

We now simplify the aircraft model introduced in the previous section to alleviate the computational effort in the Particle Filtering calculations. We consider only aircraft flying at constant altitudes and with constant speeds (i.e. trimmed flight). Since V and Z are held constant we can drop third and fourth dynamic equations of (3.2.1). Moreover we define the flight plan for each aircraft using only the initial and the final waypoint so as to avoid turns and considering only straight trajectories. Thanks to these hypothesis we can disregard the discrete part of the model and simplify the continuous part of the aircraft motion so as to obtain the following system

$$\begin{bmatrix} \dot{X} \\ \dot{Y} \\ \dot{\psi} \\ \dot{m} \end{bmatrix} = \begin{bmatrix} Vcos(\psi)cos(\gamma) + w_x \\ Vsin(\psi)cos(\gamma) + w_y \\ \frac{1}{m}\frac{Lsin(\varphi)}{Vcos(\gamma)} - W_{cgf}tan(\gamma) \\ -\eta T \end{bmatrix}$$

where L and D can be expressed as canonic-form aerodynamics forces as

$$L = \frac{C_L S \rho(Z)}{2} V^2 \quad \text{and} \quad D = \frac{C_D S \rho(Z)}{2} V^2$$

with S total wings surface, $\rho(Z)$ air density at an altitude of Z and C_D and C_L drag and lift coefficients related to the type of aircraft considered [15]. Substituting the expression of these forces we finally obtain the following dynamics:

$$\begin{bmatrix} \dot{X} \\ \dot{Y} \\ \dot{\psi} \\ \dot{m} \end{bmatrix} = \begin{bmatrix} Vcos(\psi)cos(\gamma) + w_x \\ Vsin(\psi)cos(\gamma) + w_y \\ \frac{1}{2m}\rho(Z)C_L S\frac{sin(\varphi)}{cos(\gamma)} - W_{cgf}tan(\gamma) \\ -\eta T \end{bmatrix} \tag{3.2.4}$$

Another simplification is the one proposed for the time-correlation in order to ease the implementation of the dynamics:

$$r_t(|t - t'|) \approx e^{-\frac{|t-t'|}{G_t}},$$

that is a good approximation considering the time horizon of 30 minutes hour used in our analysis (for a full explanation refer to [26]).
In order to justify in (3.2.3) the initialization of the wind vector and the covariance matrix $\hat{R}$ we can considering

$$W_x(k) = \begin{bmatrix} w_x(k, p_1) \\ \vdots \\ w_x(k, p_n) \end{bmatrix}$$

if $W_x(0) = \hat{Q}v_x(0)$ we could derive the following expression

$$\begin{aligned} E\left[W_x(0)W_x^T(0)\right] &= E\begin{bmatrix} w_x^2(0,p_1) & \dots & w_x(0,p_1)w_x(0,p_n) \\ & \ddots & \vdots \\ & & w_x^2(0,p_n) \end{bmatrix} = \\ &= \begin{bmatrix} E\left[w_x^2(0,p_1)\right] & \dots & E\left[w_x(0,p_1)w_x(0,p_n)\right] \\ & \ddots & \vdots \\ & & E\left[w_x^2(0,p_n)\right] \end{bmatrix} = \\ &= \hat{R} \end{aligned}$$

so we can say that $\hat{Q}\hat{Q}^T = \hat{R}$.

Covariance matrix dynamics is governed by (3.2.3) so:

$$E\left[W_x\left(k+1\right)W_x^T\left(k+1\right)\right] = a^2 E\left[W_x\left(k\right)W_x^T\left(k\right)\right] + QQ^T = \\ = a^2 E\left[W_x\left(k\right)W_x^T\left(k\right)\right] + \left(1-a^2\right)\hat{R}$$

At the equilibrium we have that

$$E\left[W_x\left(k+1\right)W_x^T\left(k+1\right)\right] = E\left[W_x\left(k\right)W_x^T\left(k\right)\right] \;\Rightarrow\; E\left[W_x\left(k\right)W_x^T\left(k\right)\right] = \hat{R} \quad \forall k$$

Setting $W_x\left(0\right) = \hat{Q}v_x\left(0\right)$ we initialize the system with the equilibrium value so, thanks to $0 < a < 1$, it will remain in that state absorbing possible perturbation. Values taken by $W_x\left(k\right)$ will maintain the correlation structure previously defined.
All conclusions we have just drawn for W_x are also valid for W_y thanks to the isotropicity hypotesis.
Finally concerning the radar measurements we choose to consider a "safety uncertainty" that does not depend on the distance of the aircraft from the radar using a constant standard deviation

$$\sigma_r = 80 \text{ m} \quad \forall d$$

In our work this noise affects only the X and Y measurements, because the altitude at which the aircraft is flying is supposed to be constant and perfectly known.

3.3 Particle Filtering of the aircraft measurements

Particle Filtering (PF) is a Bayesian approach to state estimation that has been developed for nonlinear systems. The goal of PF is to compute the conditional probability distribution of the state of the system given the available output observations. In the case of a linear system subject to Gaussian noise, the conditional probability distribution of the state is Gaussian and, hence, uniquely specified by its mean and covariance. As more observations become available, mean and covariance can be recursively updated through the Kalman filter equations. If the system is nonlinear (or noise is not Gaussian), then, the conditional distribution of the state is not Gaussian and cannot be finitely parameterized through mean and covariance. The idea developed

in the PF approach to Bayesian estimation is to represent probability distributions through random samples (particles) extracted from them, and to reproduce the basic steps involved in the (ideal) optimal Bayesian recursive estimation procedure by repeatedly propagating these particles through the system dynamics (prediction step) and re-sampling them based on their likelihood given the observations (conditioning step). This is explained next with reference to a general stochastic system. An improved version of the PF exploiting the specific structure of the nonlinear stochastic system under consideration in the present work is then described. This improved version was proposed in [26] and named Sequential Conditional Particle Filter.

3.3.1 Bayesian estimator

Consider a discrete time non-linear stochastic system

$$\begin{cases} x_{k+1} = f_k(x_k, w_k) \\ y_k = h_k(x_k, n_k) \end{cases}$$

with $w(\cdot)$ and $n(\cdot)$ independent stochastic processes with know probability distribution function. The aim of the Bayesian estimator is to approximate the conditional probability distribution of x_k given the measurements $y_1, \ldots, y_k$, that is $p(x_k|Y_k)$ where $Y_k = [y_1, \ldots, y_k]$. We look for a recursive procedure to calculate the conditional distribution $p(x_k|Y_k)$.
We start from

$$\begin{aligned} p(x_k|Y_{k-1}) &= \int_{\mathbb{R}^n} p([x_k, x_{k-1}]\,|Y_{k-1})dx_{k-1} = \\ &= \int_{\mathbb{R}^n} p(x_k|\,[x_{k-1}, Y_{k-1}])p(x_{k-1}, Y_{k-1})dx_{k-1} = \\ &= \int_{\mathbb{R}^n} p(x_k|x_{k-1})p(x_{k-1}|Y_{k-1})dx_{k-1} \end{aligned}$$

whose integrand is known since $p(x_{k-1}|Y_{k-1})$ is available as a result of computations at the previous $k-1$ time instant, whereas $p(x_k|x_{k-1})$ can be computed based on $f_k(\cdot,\cdot)$ and the probability distribution of $w(\cdot)$.
Since

$$p(x_k) = \frac{p(x_k|Y_{k-1})p(Y_{k-1})}{p(Y_{k-1}|x_k)}$$

we can write

$$p(x_k|Y_k) = \frac{p(Y_k|x_k)p(x_k)}{p(Y_k)} = \frac{p([y_k, Y_{k-1}]\,|x_k)}{p(y_k, Y_{k-1})}\frac{p(x_k|Y_{k-1})p(Y_{k-1})}{p(Y_{k-1}|x_k)} =$$
$$= \frac{p(Y_{k-1}|\,[x_k, y_k])p(y_k|x_k)p(x_k|Y_{k-1})}{p(y_k|Y_{k-1})p(Y_{k-1}|x_k)} = \frac{p(Y_{k-1}|x_k)p(y_k|x_k)p(x_k|Y_{k-1})}{p(y_k|Y_{k-1})p(Y_{k-1}|x_k)}.$$

Finally we obtain

$$p(x_k|Y_k) = \frac{p(y_k|x_k)p(x_k|Y_{k-1})}{p(y_k|Y_{k-1})}, \tag{3.3.1}$$

where $p(y_k|x_k)$ can be computed based on $h_k(\cdot,\cdot)$ and the probability distribution of the measurement noise $n(\cdot)$, and

$$p(y_k|Y_{k-1}) = \int_{\mathbb{R}^n} p(y_k|x_k)p(x_k|Y_{k-1})dx_k.$$

We can then calculate $p(x_k|Y_k)$ recursively starting from $p(x_0|Y_0) = p(x_0)$

3.3.2 Particle Filter

In general it is difficult to compute an analytic expression for the Bayesian estimate, since it involves representing probability distribution function and computing various integrals. The idea of PF is to use random samples to solve the issue of representing probability distributions and computing integrals. This is summarized in the following Algorithm.

1. random generation of N particles $x^+_{0,i}$ based on the initial pdf $p(x_0)$;

2. propagation of the particles to the next time step using the process equation:
$$x^-_{k,i} = f_{k-1}(x^+_{k-1,i}, w_{k-1,i})$$
where w_{k-1} is extracted at random;

3. after receiving measurements $\tilde{y}_k$ we compute the conditional relative likelihood of each particle
$$q_i = p(\tilde{y}_k|x^-_k)$$
where $p(y_k|x_k)$ is known through $h_k(\cdot,\cdot)$ and the probability distribution of $n(\cdot)$;

4. normalization the previously obtained relative likelihoods

$$q_i = \frac{q_i}{\sum_{j=1}^{N} q_j}$$

this leads to a discrete probability density function that, as $N \to \infty$, is a good approximation for $p(x_k|y_k)$;

5. resampling of N particles $x_{k,i}^{+}$ using the approximation of $p(x_k|y_k)$;

6. restart from step 2 with $k = k + 1$.

The PF algorithm may suffer of a problem known as sample impoverishment, i.e., it may happen that the *a priori* particles are distributed according to $p(x_k|y_{k-1})$ and then when we use $p(y_k|x_k)$ to re-sample them, just a few particles will survive and become *a posteriori* particles. In the worst case all of the particles will collapse to the same value. There are many solutions developed to counteract this issue such as Roughening, Prior editing, Regularized PF, Markov chain Monte Carlo resampling, Auxiliary PF [41].

3.3.3 Sequential Conditional Particle Filter

Instead of using standard PF algorithm we opt for the Sequential Conditional Particle Filter algorithm proposed in [26] to solve the wind state estimation and trajectory prediction problem. The first novelty of the algorithm in [26] is that, instead of using realizations for the wind field carried by the particles (as in conventional Particle Filtering) the entire conditional probability distribution of the wind field is stored and manipulated, since the wind evolves according to a linear model with Gaussian noise. The aircraft are treated as flying sensors providing implicitly measurements for the wind they experience. Since conditionally to the wind field the state variables of different aircraft are independent of each other, then they are sequentially processed. This is the second novelty of the algorithm. Every radar measurement contains information about the positions of all aircraft in a region of the airspace. New measurements are processed one aircraft at the time: the measurement of the position of aircraft 1 is used first to "filter" all the particles, updating the estimate of the state of aircraft 1, and the distributions of the wind field. The updated aircraft state is stored until the $k + 1$ measurement, while wind distributions are filtered using the measurement of the position of aircraft 2, then aircraft 3, and so on. It is important to underline

that the order with which measurements are analyzed is not important [26]. Let $x(k)$ denote the overall state of the system comprising 6 states (X, Y, Z, ψ, m and V with Z and V constant and known) for each aircraft flying in the airspace at the considered time instant and $W_X(k)$ and $W_Y(k)$ denote the wind vectors. It is possible to compute the state of all aircraft using the dynamics previously presented in Section 3.2. Values of the wind acting on each aircraft ($w_X(t,\ell)$ and $w_Y(t,\ell)$) are computed by linear interpolation of the wind field ($W_X(k)$ and $W_Y(k)$) as

$$w_X(t,\ell) = A(X(t,\ell), Y(t,\ell), Z(\ell))W_X(k)$$

$$w_Y(t,\ell) = A(X(t,\ell), Y(t,\ell), Z(\ell))W_Y(k)$$

where A can be explicitly computed. The state value at the following time step is completed with the update of W_X and W_Y according to (3.2.3)
At every time instant the position of all aircraft is measured by a radar that returns a measurements vector (X, Y and Z). The prediction is executed at every time instant, or better every time a measurement from the radar is available. $x(k)$ includes two classes of variables: aircraft state evolving with non-linear dynamics and wind state evolving according to linear dynamics. A great advantage of SCPF is that, unlike other PF strategies, it can handle hundreds of aircraft and 1000 particles, without presenting a too severe impoverishment of samples [26].

Algorithm 3 Sequential Conditional Particle Filter

1: `INITIALIZATION` of aircraft states from measurements;

2: `SET` $k = 0$ and `GENERATE` N particles each comprising:

- an estimate $\hat{x}_a^i(kdt, \ell)$ of the state of each aircraft flying in the airspace; `SET` $(X^i(kdt, \ell), Y^i(kdt, \ell), Z^i(kdt, \ell)) = y_a(k, \ell)$ (the measured position of aircraft ℓ at time kdt);
- an estimate of the mean (μ_X^i and μ_Y^i) and covariance matrix Σ^i of the wind states; `SET` $\mu_X^i = 0$, $\mu_Y^i = 0$ and $\Sigma^i = \hat{R}$

3: `INCREMENT` k

4: `UPDATE` aircraft list: remove state of aircraft that have left airspace between $(k-1)dt$ and kdt and insert (with corresponding initialization) aircraft that have entered the airspace;

5: `FOR` aircraft $\ell = 1 \dots M(k)$ `DO`

6: `EXTRACT` wind realization for each of N particles $W_X^i \sim \mathcal{N}(\mu_X^i, \Sigma^i)$ and $W_Y^i \sim \mathcal{N}(\mu_Y^i, \Sigma^i)$

7: `PROPAGATE` aircraft dynamics for each of N particles from $(k-1)dt$ to kdt using (3.2.4)

8: `COMPUTE` relative likelihood for each of N particles $q^i = p(y(k, \ell)|\hat{x}_a^i(kdt, \ell))$ and `NORMALIZE` $\tilde{q}^i = q^i / \sum_{i=1}^N q^i$

9: `RESAMPLE` N particles with probability of selecting particles j equal to $\tilde{q}_j$

10: `CONDITION` the wind mean and covariance matrix for each of N particles according to

$$\begin{aligned} \mu_X^i &= \mu_X^i + \Sigma^i (A^i)^T (A^i \Sigma^i (A^i)^T)^{-1} (b_X^i - A^i \mu_X^i) \\ \mu_Y^i &= \mu_Y^i + \Sigma^i (A^i)^T (A^i \Sigma^i (A^i)^T)^{-1} (b_Y^i - A^i \mu_Y^i) \\ \Sigma^i &= \Sigma^i - \Sigma^i (A^i)^T (A^i \Sigma^i (A^i)^T)^{-1} A^i \Sigma^i \end{aligned} \tag{3.3.2}$$

where $A^i = A(\hat{x}_a^i(kdt, \ell))$, $b_X^i = A^i W_X^i$ and $b_Y^i = A^i W_Y^i$

`END FOR`

11: `EVOLVE` wind dynamics for each of N particles according to

$$\begin{aligned} \mu_X^i &= a\mu_X^i \\ \mu_Y^i &= a\mu_Y^i \\ \Sigma^i &= a^2 \Sigma^i + (1 - a^2)\hat{R} \end{aligned} \tag{3.3.3}$$

12: `RETURN` to step 2

3.4 Unscented Kalman filtering of the debris measurements

In this section we propose too use the unscented Kalman filter to improve the footprint estimation in the case when some measurements of the debris position become available after the reentering object has experienced the major breakup. We start by describing the unscented Kalman filer and then its application to our context.

Unscented Kalman filter

The Extended Kalman Filter (EKF) is probably the most widely used estimation algorithm for nonlinear systems. However, more than 35 years of experience in the estimation community has shown that is difficult to implement, difficult to tune and only reliable for systems that are almost linear on the time scale of the updates. Many of these difficulties arise from its use of linearization. To overcome this limitation, the unscented transformation (UT) was developed as a method to propagate mean and covariance information through nonlinear transformations. It is more accurate, easier to implement, and uses the same order of calculations as linearization [24].
Suppose to have a description of the current state of a nonlinear system in terms of its mean value $\bar{x}$ and its covariance matrix Σ_x, the basic idea of the UT is that it is easier to approximate a probability distribution rather than a nonlinear function. This can be done by suitably choosing a set of *sigma points* so that their mean value and covariance matrix are $\bar{x}$ and Σ_x. Then the nonlinear transformation is applied to each sigma point and updated mean and covariance matrix can be derived from the cloud of transformed points. To each sigma point is associated a weight and, in order to obtain an unbiased estimate, the sum of the weight must be equal to one.
Although there are some resemblance with particle filter, the key difference is that sigma points are *not* drawn at random but they are chosen to exhibit certain properties (i.e. given mean and covariance), so that information about the distribution can be captured with a fixed, small number of data points. Moreover the weights do not have to lie in the range $(0, 1)$.
Transposing the discussion into equations, suppose to have p sigma points

$x^{(i)}$ with $i = 1, \ldots, p$ and their weights $W^{(i)}$ such that

$$\begin{aligned} \bar{x} &= \sum_{i=1}^{p} x^{(i)} \\ \Sigma_x &= \sum_{i=1}^{p} \left[x^{(i)} - \bar{x}\right] \left[x^{(i)} - \bar{x}\right]^T \\ 1 &= \sum_{i=1}^{p} W^{(i)}, \end{aligned} \tag{3.4.1}$$

in order to obtain transformed mean and covariance matrix through nonlinear function $f(\cdot)$, we apply the function to each sigma point

$$y^{(i)} = f\left(x^{(i)}\right),$$

and then we perform statistical analysis onto transformed sigma points, obtaining mean and covariance matrix as

$$\begin{aligned} \bar{y} &= \sum_{i=1}^{p} W^{(i)} y^{(i)} \\ \Sigma_y &= \sum_{i=1}^{p} W^{(i)} \left[y^{(i)} - \bar{y}\right] \left[y^{(i)} - \bar{y}\right]^T. \end{aligned} \tag{3.4.2}$$

A typical set of sigma points, presented in [24], is a symmetric set of $2n$ points lying on the $\sqrt{n}^{th}$ contour of the covariance matrix (i.e. Σ_x in (3.4.1)), where n is the dimension of the vector $\bar{x}$. This set can be expressed as

$$\begin{aligned} x^{(i)} &= \bar{x} + \sqrt{n}\left(Q_{\Sigma_x}\right)_i \\ W^{(i)} &= 1/2n \\ x^{(i+n)} &= \bar{x} - \sqrt{n}\left(Q_{\Sigma_x}\right)_i \\ W^{(i+n)} &= 1/2n, \end{aligned} \tag{3.4.3}$$

with $i = 1, \ldots, n$ and where $\left(Q_{\Sigma_x}\right)_i$ indicates the i^{th} row of Q_{Σ_x}, that is the matrix square root (i.e. Cholesky decomposition) of Σ_x, that means that $\Sigma_x = Q_{\Sigma_x}^T Q_{\Sigma_x}$. For further insights about how to select, threat and expand sigma points set, refer to [24].

UT application to recursive estimation

In order to estimate the state of a stochastic process, whose measurements are affected by random noise we can use the Unscented Kalman Filter (UKF): a revision of the popular Kalman Filter (KF), using the UT in order to improve filter accuracy and reliability, in case of nonlinear estimation.
We next present the UKF implementation for the following nonlinear dynamic system, which is affected by additive process and measurement noises with zero mean and covariance matrices Q and S respectively

$$\begin{cases} x_k = f\left(x_{k-1}\right) + d_k \\ y_k = h\left(x_k\right) + n_k \end{cases}$$

The algorithm is a slightly simplified version of the one presented in [24], since we introduce the assumption of additive noise.

Algorithm 4 Unscented Kalman Filter

1: `SET` $\mu_0 = \mu\left(0\right)$ `AND` $\Sigma_0 = \Sigma\left(0\right)$ `AND` $k = 0$
   % $\mu\left(0\right)$ and $\Sigma\left(0\right)$ are initial state mean and covariance matrix
2: `INCREMENT` k
3: `DRAW` $N = 2n$ sigma points $x_{k-1}^{(i)}$, $i = 1, \ldots, N$ from μ_{k-1} and Σ_{k-1} as suggested by equations (3.4.3)
   % n is the state space dimension
4: `SET` $\hat{x}_k^{(i)} = f\left(x_{k-1}^{(i)}\right),\ i = 1, \ldots, N$
5: `SET`
$$\tilde{\mu}_x = \sum_{i=1}^{N} W^{(i)} \hat{x}_k^{(i)}$$
$$\tilde{\Sigma}_x = \sum_{i=1}^{N} W^{(i)} \left[\hat{x}_k^{(i)} - \tilde{\mu}_x\right] \left[\hat{x}_k^{(i)} - \tilde{\mu}_x\right]^T + Q$$
6: `SET` $\hat{y}_k^{(i)} = h\left(x_k^{(i)}\right),\ i = 1, \ldots, N$
7: `SET`
$$\tilde{\mu}_y = \sum_{i=1}^{N} W^{(i)} \hat{y}_k^{(i)}$$
$$\tilde{\Sigma}_y = \sum_{i=1}^{N} W^{(i)} \left[\hat{y}_k^{(i)} - \tilde{\mu}_y\right] \left[\hat{y}_k^{(i)} - \tilde{\mu}_y\right]^T + S$$

8: `SET` $\tilde{\Sigma}_{xy} = \sum_{i=1}^{N} W^{(i)} \left[\hat{x}_k^{(i)} - \tilde{\mu}_x\right] \left[\hat{y}_k^{(i)} - \tilde{\mu}_y\right]^T$

9: `SET` $K = \Sigma_{xy}\Sigma_y^{-1}$

$\mu_k = \tilde{\mu}_x + K\left(y_k - \tilde{\mu}_y\right)$

$\Sigma_k = \Sigma_x + K\left(\Sigma_{xy}\right)$

% Classical Kalman Filter update equations

10: `ITERATE` from step 2 until data are available.

3.5 Improved estimate of the footprint and computation of the no-fly zones

After introducing the Sequential Conditioning Particle Filter (SCPF) for the wind field prediction, and the Unscented Kalman Filter (UKF) for debris trajectory estimation, in this section we propose a novel integrated algorithm that performs both filtering procedures synchronously after the first debris measurement.

This integrated algorithm returns an estimate of the a-posteriori mean and covariance of the debris state vector, at the time instant when the last measurement is available, and an estimate of mean and covariance of the wind field. These two pieces of information are then used to dramatically improve footprint estimation that can be exploited by air traffic controllers to obtain risk areas for flight altitudes of interest, by simply intersecting the footprint with a plane at the desired height.

The integrated algorithm immediately follows.

Algorithm 5 Sequential Conditional Particle Filter with Unscented Kalman Filter

1: `INITIALIZATION` of aircraft states from measurements;

2: `SET` $k = 0$ and `GENERATE` N particles each comprising:

- an estimate $\hat{x}_a^i(kdt, \ell)$ of the state of each aircraft flying in the airspace; `SET` $(X^i(kdt, \ell), Y^i(kdt, \ell), Z^i(kdt, \ell)) = y_a(k, \ell)$ (the measured position of aircraft ℓ at time kdt);
- an estimate of the mean (μ_X^i and μ_Y^i) and covariance matrix Σ^i of the wind states; `SET` $\mu_X^i = 0$, $\mu_Y^i = 0$ and $\Sigma^i = \hat{R}$

3: `INCREMENT` k

4: `UPDATE` aircraft list: remove state of aircraft that have left airspace between $(k-1)dt$ and kdt and insert (with corresponding initialization) aircraft that have entered the airspace;

5: `FOR` aircraft $\ell = 1 \dots M(k)$ `DO`

6: `EXTRACT` wind realization for each of N particles

$$W_X^i \sim \mathcal{N}(\mu_X^i, \Sigma^i) \text{ and } W_Y^i \sim \mathcal{N}(\mu_Y^i, \Sigma^i)$$

7: `PROPAGATE` aircraft dynamics for each of N particles from $(k-1)dt$ to kdt using 3.2.4

8: `COMPUTE` relative likelihood for each of N particles

$$q^i = p(y(k, \ell) | \hat{x}_a^i(kdt, \ell)) \text{ and } \texttt{NORMALIZE } \tilde{q}^i = q^i / \textstyle\sum_{i=1}^N q^i$$

9: `RESAMPLE` N particles with probability of selecting particles j equal to $\tilde{q}_j$

10: `CONDITION` the wind means and covariance matrix for each of N particles according to

$$\begin{aligned} \mu_X^i &= \mu_X^i + \Sigma^i (A^i)^T (A^i \Sigma^i (A^i)^T)^{-1} (b_X^i - A^i \mu_X^i) \\ \mu_Y^i &= \mu_Y^i + \Sigma^i (A^i)^T (A^i \Sigma^i (A^i)^T)^{-1} (b_Y^i - A^i \mu_Y^i) \\ \Sigma^i &= \Sigma^i - \Sigma^i (A^i)^T (A^i \Sigma^i (A^i)^T)^{-1} A^i \Sigma^i \end{aligned} \tag{3.5.1}$$

where $A^i = A(\hat{x}_a^i(kdt, \ell))$, $b_X^i = A^i W_X^i$ and $b_Y^i = A^i W_Y^i$

`END FOR`

11: `UPDATE` debris: initialize debris state and covariance matrix with the first radar observation (if present at kdt) and correspondent uncertainty

12: PROPAGATE debris mean and covariance matrix, according to the Unscented Kalman Filter (Algorithm 4)

13: EVOLVE wind dynamics for each of N particles according to

$$\begin{aligned} \mu_X^i &= a\mu_X^i \\ \mu_Y^i &= a\mu_Y^i \\ \Sigma^i &= a^2\Sigma^i + (1-a^2)\hat{R} \end{aligned} \tag{3.5.2}$$

14: RETURN to step 2

Potentially this algorithm can be run continuously if we consider only the presence of aircraft, but when the first measurement of a debris object occurs one air traffic controller must carefully choose the number of iteration to run, because there is a trade-off between the accuracy of the filtered trajectory and the time remaining to estimate debris footprint and issue a warning to those aircraft that are posed at risk by the reentering event.
When the air traffic controller collected enough information, he stops Algorithm 5 and store information about last computed debris mean and covariance matrix given by the Unscented Kalman Filter and wind mean and covariance matrix given by the Particle Filter. Then he run the following Algorithm 6: a slight modification of Algorithm 2, presented in Section 2.3.1

Algorithm 6 Footprint estimation from UKF and PF outputs

1: INPUT ε AND α AND η AND $\{t_j\}_{j=1,\dots,n_s}$

2: SET N AND k according to Theorem 2

3: FOR $i := 1$ TO N

4: SET $\delta^{(i)}$:= random extraction of debris initial state $\boldsymbol{x}_0^{(i)}$ from a Gaussian distribution with mean and covariance matrix obtained from UKF and random extraction of wind initial state from a Gaussian distribution with mean and covariance matrix obtained from PF particles

5: SET $\boldsymbol{x}_{t_j}^{(i)}$:= solution to (2.2.1) at time t_j when the uncertain elements are equal to $\delta^{(i)}$, with $j = 1, \dots, n_s$

END FOR

6: SET $\{A_j^\star, \boldsymbol{c}_j^\star\}_{j=1,\dots,n_s} := \arg\min \sum_{k=1}^{n_s} \log\det A_j^{-1}$

subject to: $A_j = A_j^T \succ 0,\ j = 1,\dots,n_s;$

$$\max_{j=1,\dots,n_s} (\boldsymbol{x}_{t_j}^{(i)} - \boldsymbol{c}_j)^T A_j (\boldsymbol{x}_{t_j}^{(i)} - \boldsymbol{c}_j) \leq 1, i = 1,\dots,N;$$

7: SET $V := \emptyset$ AND $p := 0$;

% V is the set of indexes of constraints violated by $\{A_j^\star, \boldsymbol{c}_j^\star\}_{j=1,\dots,n_s}$

% p is the cardinality of V

8: WHILE $p < k$

9: SET $\{i_1, i_2, \dots, i_m\} := \left\{ i : \max_{j=1,\dots,n_s} (\boldsymbol{x}_{t_j}^{(i)} - \boldsymbol{c}_j^\star)^T A_j^\star (\boldsymbol{x}_{t_j}^{(i)} - \boldsymbol{c}_j^\star) = 1 \right\}$;

10: % $\{i_1, i_2, \dots, i_m\}$ are the indexes of active constraints

11: IF $m > k - p$

12: SET $\{j_1, j_2, \dots, j_{k-p}\} :=$ $k-p$ random integers extracted from $\{1, 2, \dots, m\}$ without repetition

13: SET $R := \{i_{j_1}, i_{j_2}, \dots, i_{j_{k-p}}\} \subset \{i_1, i_2, \dots, i_m\}$

14: ELSE

15: SET $R := \{i_1, i_2, \dots, i_m\}$

END IF

% R is the set of indexes of constraints to be removed

16: SET $\{A_j^\star, \boldsymbol{c}_j^\star\}_{j=1,\dots,n_s} := \arg\min \sum_{k=1}^{n_s} \log\det A_j^{-1}$

subject to: $A_j = A_j^T \succ 0,\ j = 1,\dots,n_s;$

$$\max_{j=1,\dots,n_s} (\boldsymbol{x}_{t_j}^{(i)} - \boldsymbol{c}_j)^T A_j (\boldsymbol{x}_{t_j}^{(i)} - \boldsymbol{c}_j) \leq 1, i \in \{1,2,\dots,N\} \setminus (R \cup V);$$

17: SET $V := \left\{ i : \max_{j=1,\dots,n_s} (\boldsymbol{x}_{t_j}^{(i)} - \boldsymbol{c}_j^\star)^T A_j^\star (\boldsymbol{x}_{t_j}^{(i)} - \boldsymbol{c}_j^\star) > 1 \right\}$ AND $p := |V|$;

% V is the set of indexes of constraints violated by $\{A_j^\star, \boldsymbol{c}_j^\star\}_{j=1,\dots,n_s}$

% p is the cardinality of V

END WHILE

18: RETURN $\{A_j^\star, \boldsymbol{c}_j^\star\}_{j=1,\dots,n_s}$.

3.6 Simulation results

We consider 6 aircraft flying at constant altitude in a region of the airspace of 600 km by 600 km in the xy plane.
As shown in Figure 3.2, aircraft are divided into two sets: the first set contains 3 aircraft flying from the lower-left corner of the airspace region to the upper-right corner, while the other 3 aircraft in the second set fly from the upper-left to the lower-right corner. Nominal trajectories cross at the center of the considered airspace region, but aircraft reaching the central point at the same time are set to fly at different altitudes. More specifically, some aircraft fly at altitude 10.5 km and the others at altitude 11.5 km.
For simplicity, aircraft are supposed to fly at a nominal airspeed of 214 m/s. For all aircraft, the parameters of the dynamical model represent a Boeing 737-700, [15].
After 15 minutes of aircraft flight, a debris enters the Earth atmosphere at the altitude of 78 km with a speed of 7.1 km/s and a path angle of $-1°$. These are the nominal data for the debris initial state.
The aircraft and debris nominal positions at time $t = 15$ minutes are depicted in Figure 3.2, together with their nominal future trajectories.

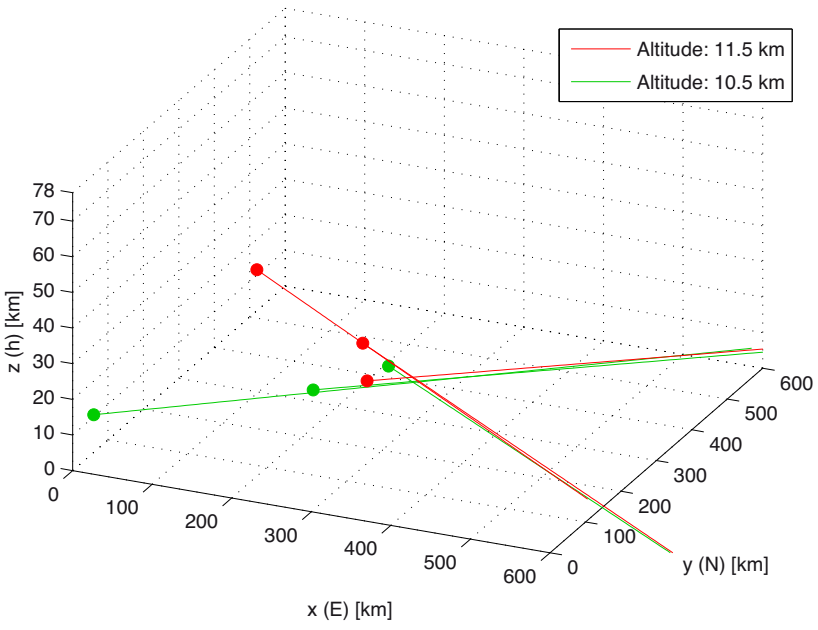

Figure 3.2: Air traffic configuration: aircraft flying at the same altitude are drawn with the same color.

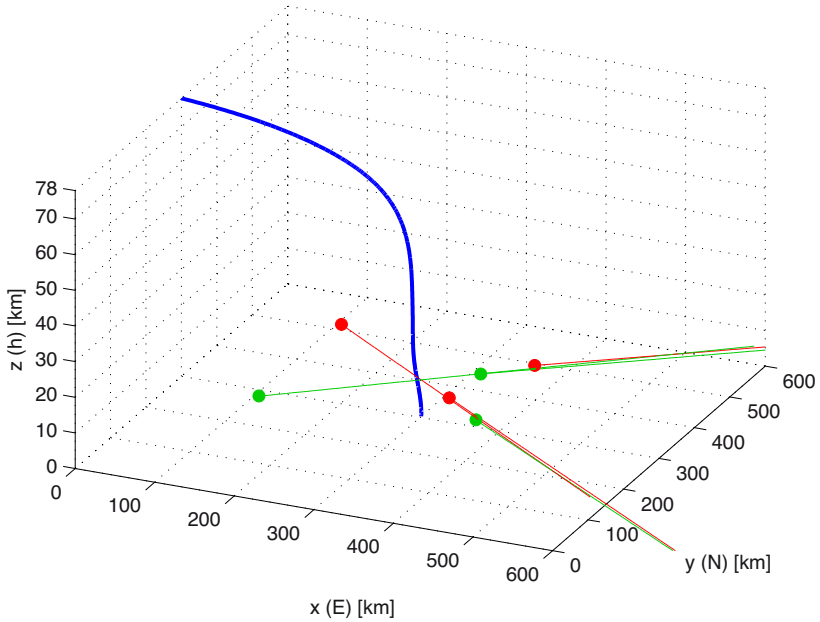

Figure 3.3: A realization of the aircraft and debris trajectories during the debris reentry.

Whiles the initial state of the aircraft is assumed to be deterministic, the initial state (position and velocity) of the debris is described as a Gaussian random variable with mean given by the nominal initial state, and variance Z_0 equal to

$$Z_0 = \begin{bmatrix} S & 0_{3\times3} \\ 0_{3\times3} & V_0 \end{bmatrix},$$

where S is the covariance matrix of the initial position (set equal to the radar noise covariance matrix), whereas V_0 is the covariance matrix of the initial velocity (set equal to that in equation (2.3.13)).
Both aircraft and debris are subject to the wind field disturbance. The nominal component of this field represents the forecasted wind and is obtained from the HWM93 model [18]. The airspace between 10 km and 12 km in altitude is also affected by a stochastic wind field component, which represents the wind forecast error and is described in Section 3.2.3.
Data representing the radar observations of the aircraft and debris positions are both available every 30 seconds. Aircraft radar measurements are corrupted by some noise, which is described as a zero-mean Gaussian process with a standard deviation of 80 m (as already discussed in Section 3.2.5).

For debris measurements, the standard deviation is raised by a factor of 2.
In order to test the performance of the proposed approach to improve the probabilistic footprint estimation based on available measurements, we can consider different scenarios corresponding to the same setup but to different stochastic wind realizations and debris initializations.
For each given scenario, we monitor the aircraft positions for 15 minutes and use the Sequential Conditional Particle Filter (SCPF) described in Section 3.3 to estimate the a-posteriori probability distribution of the stochastic wind field and aircraft state, given the aircraft radar measurements. Then, when the debris starts its reentry, we keep applying the SCPF to the aircraft radar measurements, but we also apply the Unscented Kalman Filter (UKF) in Section 3.4 to compute an estimate of the a-posteriori probability distribution of the debris state, given the debris radar measurements. In particular, we consider additional 2 minutes, corresponding to 5 radar measurements and 4 filtering steps. The probabilistic footprint is then computed based on the obtained a-posteriori probability distributions of the wind field (represented through the particles of the SCPF) and of the debris state (represented though the mean and variance of the UKF), by projecting into the future a suitable number N of debris trajectories, depending on the desired ε violation, but also on the values chosen for α and η (see Theorem 2). Here, we set $\varepsilon = 0.02$, $\alpha = 0$, and $\eta = 10^{-5}$. The number of particles in the SCPF implementation is 500.
We next consider two representative scenarios and perform the filtering and projection procedure just described. For comparison purposes we compute the footprint also in a *best-case* and in a *worst-case*.
In the best-case, we use the actual debris state and the actual wind field after 17 minutes of aircraft flight to project into the future the N debris trajectories.
In the worst-case, we neglect the information brought by the aircraft radar measurements and apply only the UKF to the debris radar measurements. We then project into the future N debris trajectories using the output of the UKF to sample the debris state at time $t = 17$ minutes, while generating the stochastic wind randomly starting from mean and covariance matrix defined in Section 3.2.3.
In all cases, we integrate debris and wind dynamics (see Sections 2.2.2 and 3.2.5) until the debris reaches a low altitude (10 km).

Simulations were carried out by first running Algorithm 5. We set the number of particles equal to 500, the time interval between two subsequent radar measurement to 30 seconds. We initialize the aircraft state $\hat{x}_a^i(0,\ell)$ in each particle i with the first radar measurement $y_a(0,\ell)$, $\forall \ell = 1,\ldots,N_a$, where $N_a = 6$ is the number of aircraft in our setup. Algorithm 5 take also into account the altitude of each aircraft that, in our case is held constant because of the level flight assumption. For the initialization of the rest of the state vector, ψ is initialized so as to make the aircraft heading to the second way point, while the initial mass is set to $m = 46000$ kg, according to [15]. As for the means μ_X^i and μ_Y^i of the wind states of each particle i, we set them to zero, whereas the covariance matrix Σ^i is set equal to $\hat{R}$.
At $k = 30$ (i.e. after $kdt = 15$ minutes of simulation) we initialize the Unscented Kalman Filter mean and covariance matrix with the first radar measurement $y_{de}(k)$ of the debris position and the initial covariance matrix Z_0, respectively.
The process noise matrix Q in Algorithm 4 is set equal to

$$Q = \begin{bmatrix} 0_{3\times3} & 0_{3\times3} \\ 0_{3\times3} & \Xi \end{bmatrix}$$

where Ξ is the covariance matrix of $\boldsymbol{\xi}$ in (2.2.1) and is set equal to

$$\Xi = \begin{bmatrix} 2.4064\cdot10^{-5} & 0 & 0 \\ 0 & 2.4064\cdot10^{-5} & 0 \\ 0 & 0 & 2.4064\cdot10^{-5} \end{bmatrix}$$

as suggested in [24]. The covariance matrix S for the measurement noise is set equal to

$$S = \begin{bmatrix} 160 & 0 & 0 \\ 0 & 160 & 0 \\ 0 & 0 & 160 \end{bmatrix}.$$

At the end of the iteration $k = 34$, we collect wind mean and covariance matrix of all particles along with debris mean and covariance matrix, and initialize Algorithm 6 with these quantities so as to make it extract realizations of the uncertainty affecting the debris according to the a-posteriori probability distributions estimated through Algorithm 5.
Results achieved in the best-case, worst-case, and with the approach using

both SCPF and UKF are presented in the following figures. Each figure refers to one of the two considered scenarios: footprints obtained in best-case are depicted in red, those obtained in the worst-case are in green, and those built by applying our approach are in blue. We also plot with a black solid line the debris trajectory of the considered scenario.

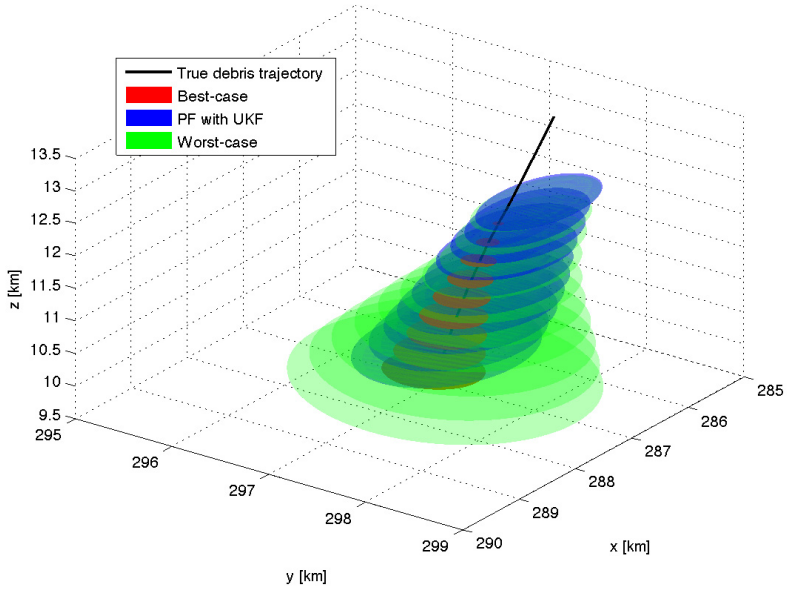

Figure 3.4: Footprint comparison - Scenario 1

In both scenarios, the debris trajectory belongs to the footprint obtained with the proposed approach. Also, as expected, the volume of the footprint is lower bounded by that obtained in the best-case and upper-bounded by that in the worst-case. Table 3.1 quantifies the volume reduction with respect to the worst-case.

Scenario	V^{worst}	V^{PF+UKF}	$\Delta_{\%}$
1	1.9143 km^3	0.8868 km^3	-53.68%
2	1.4207 km^3	0.8224 km^3	-42.12%

Table 3.1: Decreasing volume after filtering

This reduction of volume with respect to the worst-case is easily justified if one considers the performance of the SCPF in reducing the uncertainty on the wind forecast errors. To this order, in Figure 3.6 we plot the variance of

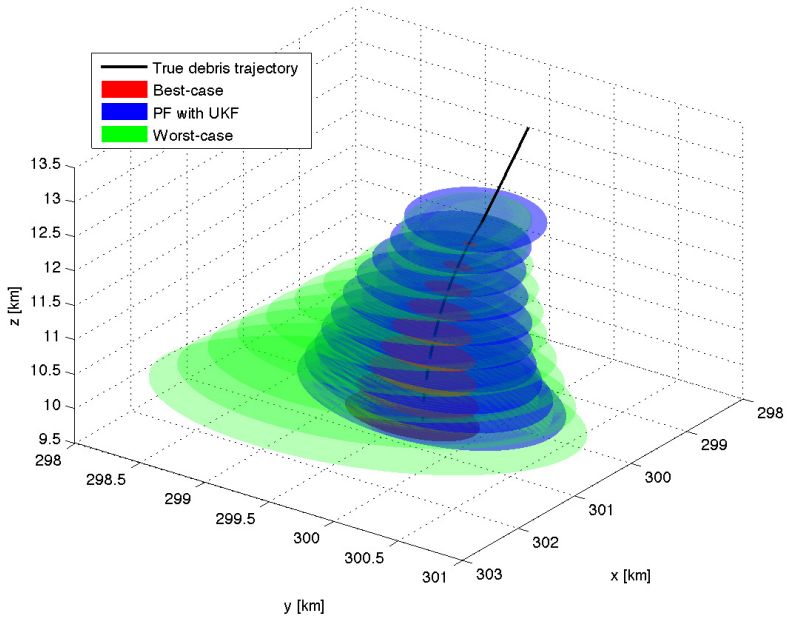

Figure 3.5: Footprint comparison - Scenario 2

the wind speed vector associated with the grid points (x, y) at the altitude of 11 km before and after applying the SCPF. As the reader can see after only 17 minutes, wind variances have been successfully lowered by almost a factor of two everywhere in the airspace.

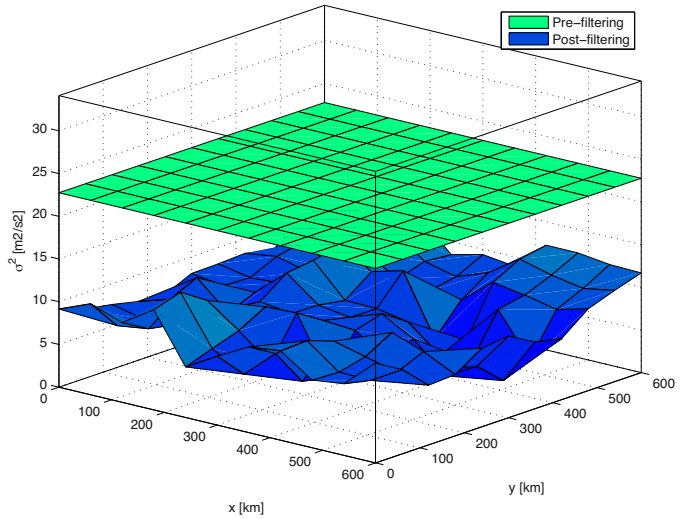

Figure 3.6: Wind field covariance matrix before and after filtering.

The region obtained by intersecting the footprint and the horizontal plane at the altitude where an aircraft is flying can be defined as no-fly region and used by air traffic controllers to take appropriate actions for conflict resolution. Figure 3.7 represents the no-fly zones for the aircraft flying at altitude 11.5 km obtained with our algorithm. The extent of such regions can be "tuned" by varying ε, at the price of incurring into a higher risk if ε is increased.

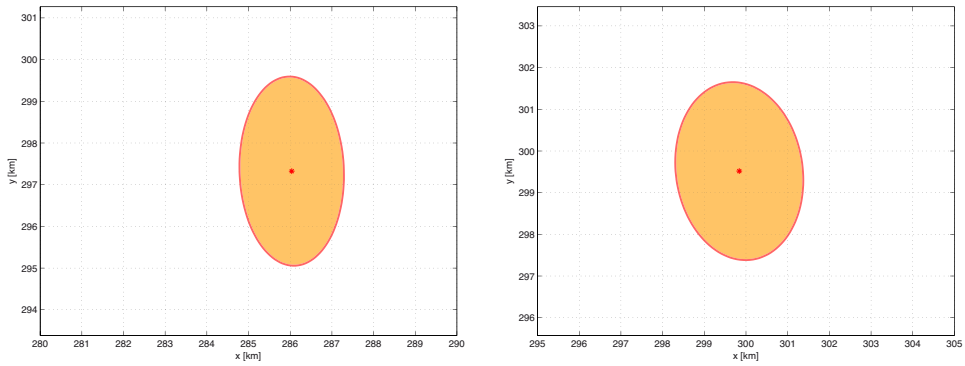

Figure 3.7: No-fly zone at altitude 11.5 km for scenario 1 (left) and scenario 2 (right).

Chapter 4

Conclusions and Outlook

4.1 Conclusions

This work has studied the problem of estimating the area of the airspace posed at risk by a reentering space debris. After a brief overview of the state-of-the-art of this active research field, we proposed a novel simulation-based approach, in order to obtain a probabilistic footprint of the 4D hazardous region, and we compared it with the covariance propagation method recently proposed in the literature. We showed that our approach outperforms the covariance propagation method, since it provides a smaller footprint, when the violation is the same. We also discussed the possibility for our technique to incorporate various source of uncertainties, and presented an example where stochastic wind is accounted for.
We then focused on the possible improvement of such footprint, demonstrating how the availability of measurements of the debris position after its breakup instant can significantly reduce the estimated spread of the debris trajectories. The Unscented Kalman Filtering technique serves this purpose. In our simulations we also experienced that, as stated in the literature, we cannot use the Particle Filter because of the sample impoverishment issue.
After having introduced the dynamics of the air traffic, comprising a model for the single aircraft, the Flight Management System and a stochastic wind model, we exploited a technique presented in the literature that uses a variant of the Particle Filter in order to estimate the true state of the wind in a certain volume of the airspace. We used these information, alongside with the Unscented Kalman Filter, to reduce the effect of wind uncertainty on debris dynamics and, hence, the overall volume of the footprint.

Results obtained in our work show that randomized techniques can be quite effective means for addressing interesting and challenging problems involving nonlinear complex dynamics. In particular, the scenario approach for solving chance-constrained optimization problems enabled us to develop the simulation-based method for the footprint characterization, whereas the sequential conditional Particle Filter jointly with the Unscented Kalman Filter allowed us to reduce the uncertainty affecting the debris, thus reducing the size of the footprint. Obviously a more in-depth analysis is required to fully validate the proposed approach, for instance by using extensive simulations to compare its performance with that of the worst-case and best-case.

4.2 Future Work

Finally, we would like to present some possible extensions of our work and interesting research directions that, in our opinion, deserve consideration.

Risk assessment

The first extension of our work concerns the implementation of an algorithm for evaluating the risk of the debris entering the protection zone of an aircraft. This can be done by Monte Carlo simulation, based on the footprint as explained in Section 2.3.4, and using the SCPF output to project the aircraft positions into the future.

Debris footprint

One of the key feature of our work is that the introduced simulation-based approach to footprint estimation allows to account for various sources of uncertainty. It would then be interesting to explore the footprint sensitivity to the different uncertainty sources so as to understand what is the most critical one.
Another interesting direction of research could be to consider the breakup event as the starting point for the simulation of a debris cloud. By generating more fragments all together and computing the overall footprint, one can characterize the region of the airspace affected by the debris cloud in toto. A further possible extension comprises the introduction of thermal analysis in order to estimate demise or survival of a fragment.

Aircraft model

Regarding aircraft modeling, a natural extension of our work would be the use of the full six-dimensional model of the aircraft instead of the simplified four-dimensional one. Variations of altitude and/or speed are of primarily importance for an air traffic controller while defining flight plans and resolution strategies. The complete model will involve accounting also for the flight management system and, hence, the discrete component of the resulting stochastic hybrid model.

Conflict Resolution

All the above mentioned possible extensions of our work aim at achieving a better estimate of the position of aircraft and debris so as to guarantee adequately accurate risk figures for the aircraft. An improved knowledge of the state of the whole system (i.e. aircraft, wind and debris) can help authorities and air traffic controllers in redefining safe flight plans when an uncontrolled reentry occurs. This calls for the introduction of appropriate 'conflict resolution' algorithms steering the aircraft away from the hazard debris area while keeping them at a safe distance one from the other.

Final considerations

In conclusion there is a lot of research that can be done in this field, and we only scratched the surface. We believe that our work is a small step towards a direction that can offer interesting research hints to the problem of aircraft risk estimation in case of uncontrolled space debris reentry.

Bibliography

[1] *U.S. Standard Atmosphere 1976.* National Oceanic and Atmospheric Administration (NOAA) and National Aeronautics and Space Administration (NASA), Washington, DC, USA, 1976.

[2] *Handbook of geophysics and the space environment.* Air Force Geophysics Laboratory, 1985.

[3] Flight safety analysis. Technical Report 1.0, Federal Aviation Administration (FAA), Washington, DC, USA, 2011.

[4] Challenge of growth 2013. task 4: European air traffic in 2035. Technical report, European Organisation for the Safety of Air Navigation (EUROCONTROL), 2013.

[5] William Ailor and Paul Wilde. Requirements for warning aircraft of reentering debris. Technical report, International Association for the Advancement of Space Safety, 2008.

[6] T. Alamo, R. Tempo, and A. Luque. On the sample complexity of randomized approaches to the analysis and design under uncertainty. pages 4671–4676, Baltimore, MD, USA, June 2010.

[7] Luciano Anselmo and Carmen Pardini. Satellite reentry predictions for the Italian civil protection authorities. In *63rd International Astronautical Congress*, Naples, Italy, 2013. International Astronautical Federation (IAF).

[8] Stephen Boyd. *Convex Optimization.* Cambridge University Press, 2004.

[9] G. Calafiore and M.C. Campi. Uncertain convex programs: randomized solutions and confidence levels. *Mathematical Programming*, 102(1):25–46, 2005.

[10] G. Calafiore and M.C. Campi. The scenario approach to robust control design. *IEEE Transactions on Automatic Control*, 51(5):742–753, 2006.

[11] Marco C. Campi, Simone Garatti, and Maria Prandini. The scenario approach for systems and control design. *Annual Reviews in Control*, 33(2):149–157, 2009.

[12] M.C. Campi, G. Calafiore, and S. Garatti. Interval predictor models: identification and reliability. *Automatica*, 45:382–392, 2009.

[13] M.C. Campi and S. Garatti. The exact feasibility of randomized solutions of robust convex programs. *SIAM Journal on Control and Optimization*, 19(3):1211–1230, 2008.

[14] M.C. Campi and S. Garatti. A sampling-and-discarding approach to chance-constrained optimization: feasibility and optimality. *Journal of Optimization Theory and Applications*, 148(2):257–280, 2011.

[15] EUROCONTROL. *User Manual for the Base of Aircraft Data*, 3.10 edition, 2012.

[16] Michael V. Frank, Michael A. Weaver, and Richard L. Baker. A probabilistic paradigm for spacecraft random reentry disassembly. *Reliability Engineering and System Safety*, 90(2-3):148–161, 2005.

[17] Michael D. Griffin and James R. French. *Space Vehicle Design*. AIAA education series. Americal Institute of Aeronautics and Astronautics, Inc., Reston, Virginia, USA, 1991.

[18] A.E. Hedin, E.L. Fleming, A.H. Manson, F.J. Schmidlin, S.K. Avery, R.R. Clark, S.J. Franke, G.J. Fraser, F. Vial T. Tsuda, and R.A. Vincent. Empirical wind model for the upper, middle and lower atmosphere. *Journal of Atmospheric and Terrestrial Physics*, 58(13):1421–1447, 1996.

[19] Haitham Hindi. A tutorial on convex optimization.

[20] Jianghai Hu, Maria Prandini, and Shankar Sastry. Optimal coordinated maneuvers for three-dimensional aircraft conflict resolution. *Journal of Guidance, Control and Dynamics*, 25:888–900, 2012.

[21] Jian Huang, Weidong Hu, Qin Xin, and Weiwei Guo. A novel data association scheme for LEO space debris surveillance based on a double fence radar systems. *Advances in Space Research*, 50(11):1451–1461, 2012.

[22] Richard Irvine. The gears conflict resolution algorithm. In *AIAA Guidance, navigation and control Conference*. American Institute of Aeronautics and Astronautics, 1998.

[23] Richard Irvine. Comparison of pair-wise priority-based resolution schemes through fast-time simulation. In *8th Innovative Research Workshop and Exhibition*. EUROCONTROL Experimental Centre, 2009.

[24] Simon J. Julier and Jeffrey K. Uhlmann. Unscented filtering and nonlinear estimation. In *Proceedings of the IEEE*, volume 92, 2004.

[25] Kuchar and Yang. A review of conflict detection and resolution modeling methods. *IEEE Transactions on Intelligent Transportation Systems*, 1:179–189, 2000.

[26] Ioannis Lymperopoulos. *Sequential Monte Carlo Metohds in Air Traffic Management*. PhD thesis, ETH, Zurich - Department of Information Technology and Electrical Engineering, 2010.

[27] Ioannis Lymperopoulos and John Lygeros. Adaptive aircraft trajectory prediction using particle filters. In *AIAA Guidance, Navigation and Control Conference and Exhibit*. American Institute of Aeronautics and Astronautics, 2008.

[28] Ioannis Lymperopoulos and John Lygeros. Sequential monte carlo methods for multi-aircraft trajectory prediction in air traffic management. *International Journal of Adaptive Control and Signal Processing*, 24:830–849, 2010.

[29] Michael McWinnie. Health monitoring of reentry vehicles. Master's thesis, Lulea University of Technology - Department of Computer Science, Electrical and Space Engineering, 2012.

[30] Kenneth Moe and Mildred M. Moe. Gas-surface interactions and satellite drag coefficients. *Planetary and Space Science*, 53(8):793–801, 2005.

[31] Carmen Pardini and Luciano Anselmo. Computational methods for reentry trajectories and risk assessment. *Advances in Space Research*, 35(7):1343–1352, 2005.

[32] Carmen Pardini and Luciano Anselmo. Reentry predictions of three massive uncontrolled spacecraft. In NASA/JPL, editor, *ISSFD-2012 - 23rd International Symposium on Space Flight Dynamics*, Pasadena, California, USA, 2012.

[33] Carmen Pardini and Luciano Anselmo. Reentry predictions for uncontrolled satellites: results and challenges. In *6th IAASS Conference - Safety is Not an Option*, Montréal, Canada, 2013.

[34] Russell P. Patera. Risk to commercial aircraft from reentering space debris. In *AAIA Atmospheric Flight Mechanics Conference*, 2008.

[35] Maria Prandini, Luigi Piroddi, and John Lygeros. A two-step approach to aircraft conflict resolution combining optimal deterministic desigh with monte carlo stochastic optimization. In *European Control Conference*, 2009.

[36] A. Prèkopa. *Stochastic Programming.* Kluwer, Boston, MA, 1995.

[37] A. Prèkopa. Probabilistic programming. In A. Ruszczyǹski and A. Shapiro, editors, *Stochastic Programming*, volume 10 of *handbooks in operations research and management science*, London, UK, 2003. Elsevier.

[38] R.E.Cole, C.Richard, S.Kim, and D.Bailey. An assessment of the 60 km rapid update cycle (ruc) with near real-time aircraft reports. Technical report, National Aeronautics and Space Administration (NASA), July 1998.

[39] Mahmut Reyhanoglu and Juan Alvarado. Estimation of debris dispersion due to a space vehicle breakup during reentry. *Acta Astronauta*, 86:211–218, 2013.

[40] Arrun Saunders, Hugh G. Lewis, and Graham G. Swinerd. A new tool for satellite reentry predictions. In *5th European Conference on Space Debris*, Darmstadt, Germany, 2009. European Space Agency.

[41] Dan Simon. *Optimal State Estimation: Kalman, H Infinity, and Nonlinear Approaches*. Wiley, 2006.

[42] Patricia Grace Smith. Expected casualty calculations for commercial space launch and reentry missions. Advisory Circular 431.35-1, Federal Aviation Administration (FAA), U.S. Department of Transportation, 2000.

[43] Peng Sun and Robert M. Freund. Computation of minimum-volume covering ellipsoids. *Operations Research*, 52(5):690–706, 2004.

[44] Michael J. Todd and E. Alper Yildirim. On Khachiyan's algorithm for the computation of minimum-volume enclosing ellipsoids. *Discrete Applied Mathematics*, 155:1731–1744, 2007.

[45] Michael A. Weaver, Richard L. Baker, and Michael V. Frank. Probabilistic estimation of reentry debris area. *ESA SP-473*, 2:515–520, 2011.

[46] Ziniu Wu, Ruifeng Hu, Xi Qu, Xiang Wang, and Zhe Wu. Space debris reentry analysis methods and tools. *Chinese Journal of Aeronautics*, 24(4):387–395, 2011.